University of Stavanger

Faculty of Science and Technology

MASTER'S THESIS

Study program/Specialization: Petroleum Geosciences Engineering	Spring semester, 2017 Open
Author: André Solvang	…… (signature of author)
Supervisor(s): Udo Zimmerman	
Title of master's thesis: High-resolution heavy mineral studies on "black sands" from the Nama Group (Fish River Subgroup) in Namibia – Part II.	
Credits: 30	
Key words: Nama Group (Fish River Subgroup) Heavy minerals Placer deposits Black sands Provenance Field Emission Gun Scanning Electron Microscope (FEG-SEM) X-Ray Diffractometer (XRD) Mineral Liberation Analyzer (MLA)	Number of pages: …… + supplemental material/other: …… Stavanger, …… Date/year

High-resolution heavy mineral studies on “black sands” from the Nama Group (Fish River Subgroup) in Namibia – Part II

By

André Solvang

Master’s thesis

Presented to the Faculty of Science and Technology

The University of Stavanger

The University of Stavanger

June 2017

Acknowledgements

I would like to express my gratitude towards my supervisor Dr. Udo Zimmermann at the University of Stavanger for offering me the opportunity to write this exciting master's thesis. Your genuine interest in the field of geosciences has been a true inspiration throughout the last five years during lectures and excursions. Thank you for all the support and motivation you have given me.

Also, a special thanks to Caroline Ruud and Mari Kristjansdottir for helping me with preparation of the heavy mineral mounds, which were to be analyzed. In that regard, I would also like to express my appreciation to Mona Minde for the knowledge you have provided with regards to the Field Emission Gun Scanning Electron Microscope and X-ray Diffraction at the University of Stavanger. Your guidelines and expertise in the semi-quantitative field have been very useful.

Furthermore, I wish to thank Alexandra Myhre and Sigrid Øxnevad for their great effort to perform MLA analyses in Freiberg in my absence. Completing this thesis could not have been done without you. Also, thank you Prof. Bernhard Schultz and Sabine Haser at TU Bergakademie in Freiberg for assisting my two colleges with the analyses.

Finally, I would like to thank my dear wife, Silje, and the rest of my family. Your never-ending support and encouragement have helped me overcome any challenges that life has brought. I am forever grateful for calling you my family.

Table of content

List of Tables

List of Figures

Often used abbreviations

UiS = University of Stavanger

HM: Heavy Minerals

XRD = X-Ray Diffraction

FEG-SEM = Field Emission Gun Scanning Electron Microscope

SE = Secondary Electron

BSE = Backscattered Electron

EDS = Energy Dispersive Spectrometry

CL = Cathodoluminescent

MLA = Mineral Liberation Analyzer

My = Million years

Wt% = Weight percent

Mf = Magnetic fraction

Af = Apatite fraction

Zf = Zircon fraction

Abstract

"Black sands" from a presumed heavy mineral placer of the Nama Group in Namibia will be studied in detail. The samples for this thesis are collected from various outcrops belonging to the Fish River Subgroup in the Nababis Formation. This formation lies in the Nama Basin, in which the Haribes Member is deposited. High-resolution heavy mineral stratigraphy for the succession will be used to determine provenance of the detrital material. To achieve this, a methodical approach will be used where geochemistry, XRD (X-Ray Diffraction), and semi-quantification of heavy minerals using MLA (Mineral Liberation Analyzer) are combined with FEG-SEM-BSE-EDS-CL (Field Emission Gun Scanning Electron Microscope, Back Scattered Electron, Energy Dispersive Spectrometer and Cathodoluminescence).

Heavy mineral size distribution suggests normal size distribution with peaks around 125-150 microns for all samples, with one exception, Zf 409, which has bimodal size distribution in the range of 75 – 125 microns. Furthermore, all heavy mineral particles are generally angular to sub-angular, which can infer a short transportation route. The samples display relative similar mineralogy according to FEG-SEM and MLA analyses. One can suggest a proximal metamorphic source based on findings of i.e. chamosite, garnets, clinopyroxene, as well as the possibility of the identified grossular are Ca-epidotes according to XRD analysis. Moreover, the chemical composition of garnets was plotted in ternary diagrams, which show evidence of amphibolite facies and metabasic rock associations.

Provenance studies can be very useful to determine the tectonic setting of the sedimentary successions and the detrital material. By determining the main characteristics of the depositional basins and the source areas of the deposited detritus, it is possible to understand sedimentological processes. This is one of the important sources of information for the mineral and petroleum industry that need to evaluate potential plays.

Introduction

1.1. Objectives

This thesis is a part of a bigger research project supervised by Dr. Udo Zimmermann. The main objective is to perform detailed heavy mineral studies of the retrieved samples of the Haribes Member in the Nababis Formation (Table 1). to increase the geological knowledge of the area, including sedimentary, tectonic, and metamorphic processes. Based on comparison of the results from conducted XRD, MLA and FEG-SEM analyses, evaluation of the heavy mineral distribution can be performed. Other methods, i.e. whole rock geochemistry, zircon age dating and petrography in form of thin sections are not available for this thesis due to limited time and resources.

Provenance of the heavy minerals will be discussed based on these findings and the facies association of detritus material, if possible. Finally, by gaining a better understanding of how the Nama Basin developed, parallels between the South African coast and South America may be drawn. Finally, one will try to answer if the selected placer deposits give a different provenance result than those, which are available in the literature and related to the normal background sedimentation.

TRADITIONAL LITHOSTRATIGRAPHY		
Formations	N Members	S
GROSS AUB FORMATION	Deurstamp Member	
	Rosenhof Member	
NABABIS FORMATION	Haribes Member	
	Zamnarib Member	
BRECKHORN FORMATION		
STOCKDALE FORMATION	Wasserfall Member	
	Inachab Member	
	Haseweb Mb.	
	Kabib Mb.	

Table 1: Traditional lithostratigraphy after Germs (1983).

1.2. Sampling and methodology

The project area lies in southeastern Namibia, roughly 100 km North from Orange River. A total of four samples were collected from an outcrop approximately 60 km South East from Keetmanshoop. Here, one can find the formation of interest; the Nababis Formation in which the Haribes Member is located. It is situated stratigraphically in Lower Cambrian time.

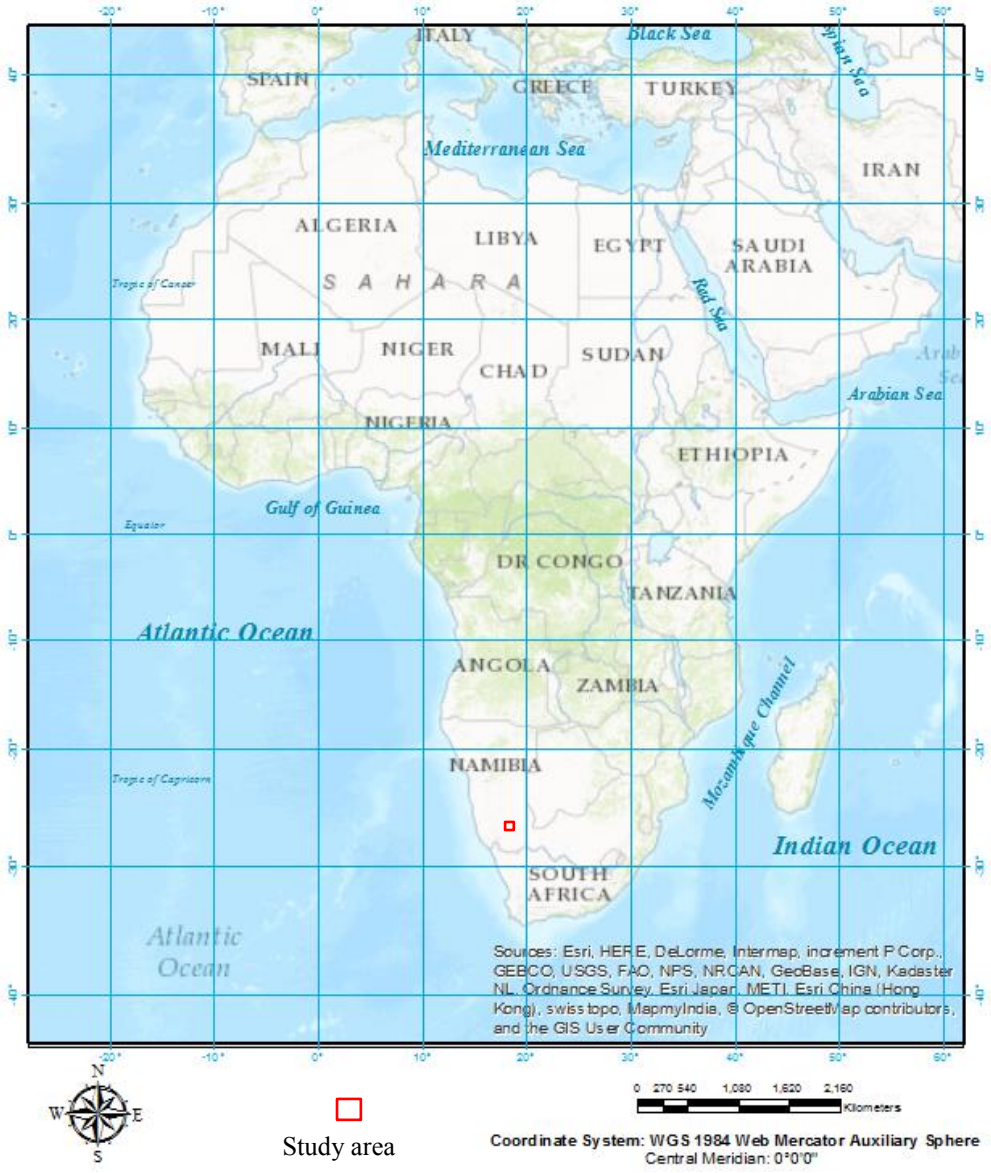

Figure 1: Map illustrating the research area in Namibia.

The following samples are separated into three fractions. A magnetic fraction that includes magnetic grains with a specific density above 2.75g/cm^3. Furthermore, the apatite fraction comprises non-magnetic grains with a specific density between 2.75 and 3.3 g/cm3. The third fraction is the zircon fraction, which includes grains with a specific density above 3.3 g/cm3 (Table 2).

Table 2: Overview of the separated mineral fractions.

Sample	Location	Fraction	Formation	Member
412	S26 55' 04,2' E18 36' 15,9''	Magnetic	Nababis	Haribes
		Apatite		
		Zircon		
409	300 m from outcrop 412	Magnetic		
		Apatite		
		Zircon		
408	300 m from outcrop 412	Magnetic		
		Apatite		
		Zircon		
405	300 m from outcrop 412	Magnetic		
		Apatite		
		Zircon		

1.3. Working Title of the study and procedures

High-resolution heavy mineral studies on “black sands” from the Nama Group (Fish River Subgroup) in Namibia – Part II.

The subject of matter is the Haribes Member of the Nababis Formation near Keetmanshoop that was collected in 2004/2005 by Professor Udo Zimmermann and in turn separated in Australia. The following XRD- and SEM- analysis were completed at the University of Stavanger, while MLA was performed in Freiberg, Germany. A proposed workflow is given below (Figure 2).

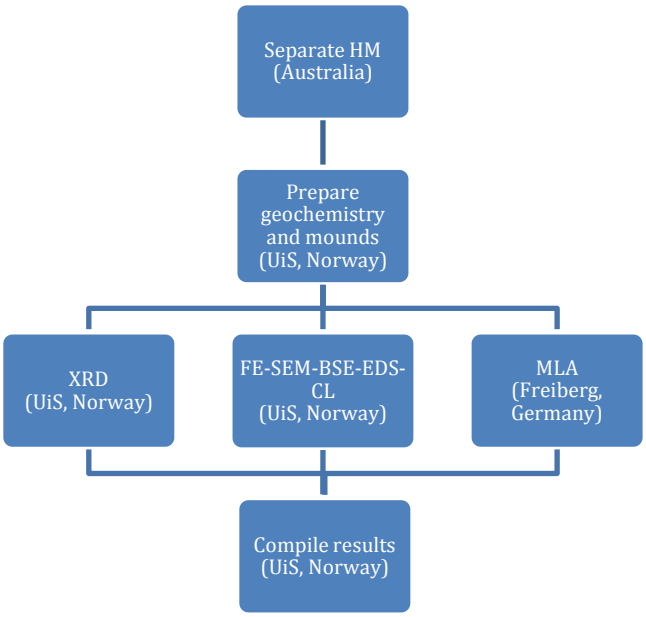

Figure 2: Workflow for the thesis.

1.4. Outline of study

This thesis will give an overview of the geological settings near the Nama Basin in Southeastern Namibia to point out important events in geological terms. Furthermore, the methodology with regards to the process of preparing the various samples for analyses carried out with XRD, MLA and FEG-SEM will be introduced. Moreover, findings of the heavy mineral rich "black sands" placer deposits of the Haribes Member in the Nababis Formation will be presented.

1.5. Geological & tectonic setting

The Nama Group was deposited in a peripheral foreland basin (Germs and Gresse, 1991; Germs, 1995; Grotzinger et al., 1995). It is today located on the eastern edge of the Kalahari Craton and borders the northern Damara and the eastern Gariep Pan-African orogenic belts (Davies and Coward, 1982; Miller, 1983). The foreland basin can be divided into three sub-basins separated by east-west- trending ridges or arches that developed while the orogenic belts were subjected to deformation. The Zaris and Witputs sub-basins are in Namibia, whereas the

Vanrhynsdorp lies in South Africa (Figure 3). The Zaris basin and Witputs basin are segregated by the Osis Ridge, whereas the Witputs basin and the Vanrhynsdorp basin are divided by the Kamieskroon Ridge (Gresse and Germs, 1993).

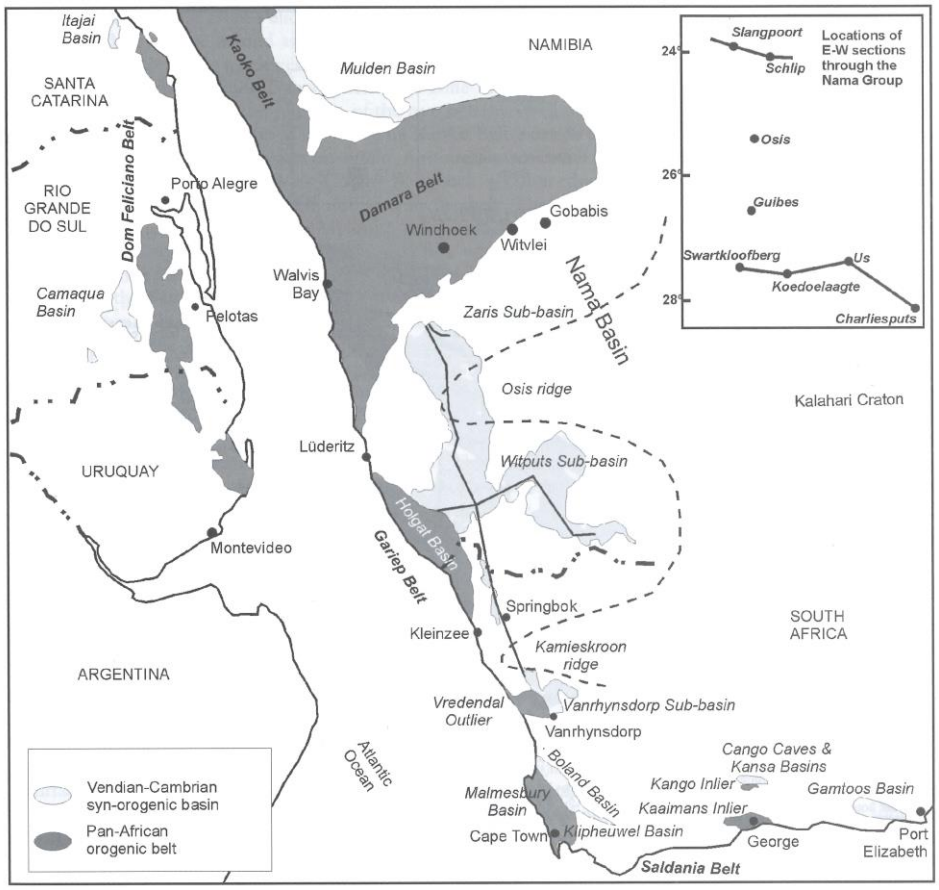

Figure 3: Position of the Pan-African orogenic belts and corresponding basins in southwestern Africa and their counterparts in southeastern South America. In the top right corner, one can see the locations of east-west cross-sections through the Nama Basin (Taken

The Damara Orogeny and the Gariep Orogeny that took place during Late Neoproterozoic – Early Cambrian is believed to be responsible for the development of the Nama foreland basin. This is roughly constrained to 550 – 530 Ma (Germs and Gresse, 1991; Germs, 1995; Geyer, 2005). Rifting and break-up of a supercontinent occurred during the Neoproterozoic – Early Cambrian (that was formed ~1.0 Ga) and further subduction and collision of Kalahari, Congo, Rio de la Plata, and Malvinas plates (Figure 3) contributed to deposition of the Neoproterozoic rocks of the Nama Basin (Dalziel, 1991; Gray et al., 2006; Gresse, 1992; Miller, 1983). The

sediments reflect Winson cycles (Germs, 1995) due to closing of two oceanic arms named the Adamaster Ocean and the Khomas Sea (Germs and Gresse, 1991; Geyer, 2005). Ar-Ar ages on amphiboles in mafic rocks in the oceanic Marmora Terrane, suggests that closure of the Adamaster Ocean was underway at 574 ± 9 Ma (Frimmel and Frank, 1998). Additional constrains by Ar-Ar muscovite ages suggest that final closure of the Adamaster Ocean started around 545 Ma (Frimmel and Frank, 1998).

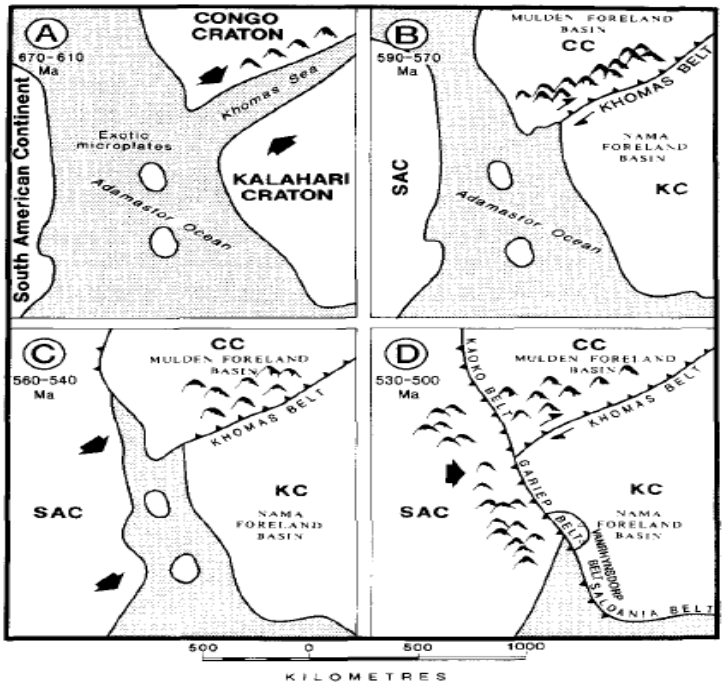

Figure 4: Cratonic movements during closure and colliding of the Khomas Sea and Adamastor Ocean (Stanistreet et al., 1991), taken from (Germs, 1995).

An Andean-type margin was created on the Congo Craton when the Kalahari Craton rotated clockwise with respect to the Congo Craton. Conversely, the Kalahari Craton shows passive margin sedimentation (Stanistreet et al., 1991). Parts of the fold-and-thrust belt that derived from the collision of the two cratons were transported southwards and formed the Osis Ridge, resulting in a peripheral foreland (Figure 4) that is indicative of the lower Nama Group sedimentary basin (Germs and Gresse, 1991; Geyer, 2005; Gresse and Germs, 1993). During the time of deposition, shallow marine, often calcareous units, developed in marine environments of the western basin, whereas a fluvial clastic belt developed along the peripheral margin in the east (Germs and Gresse, 1991).

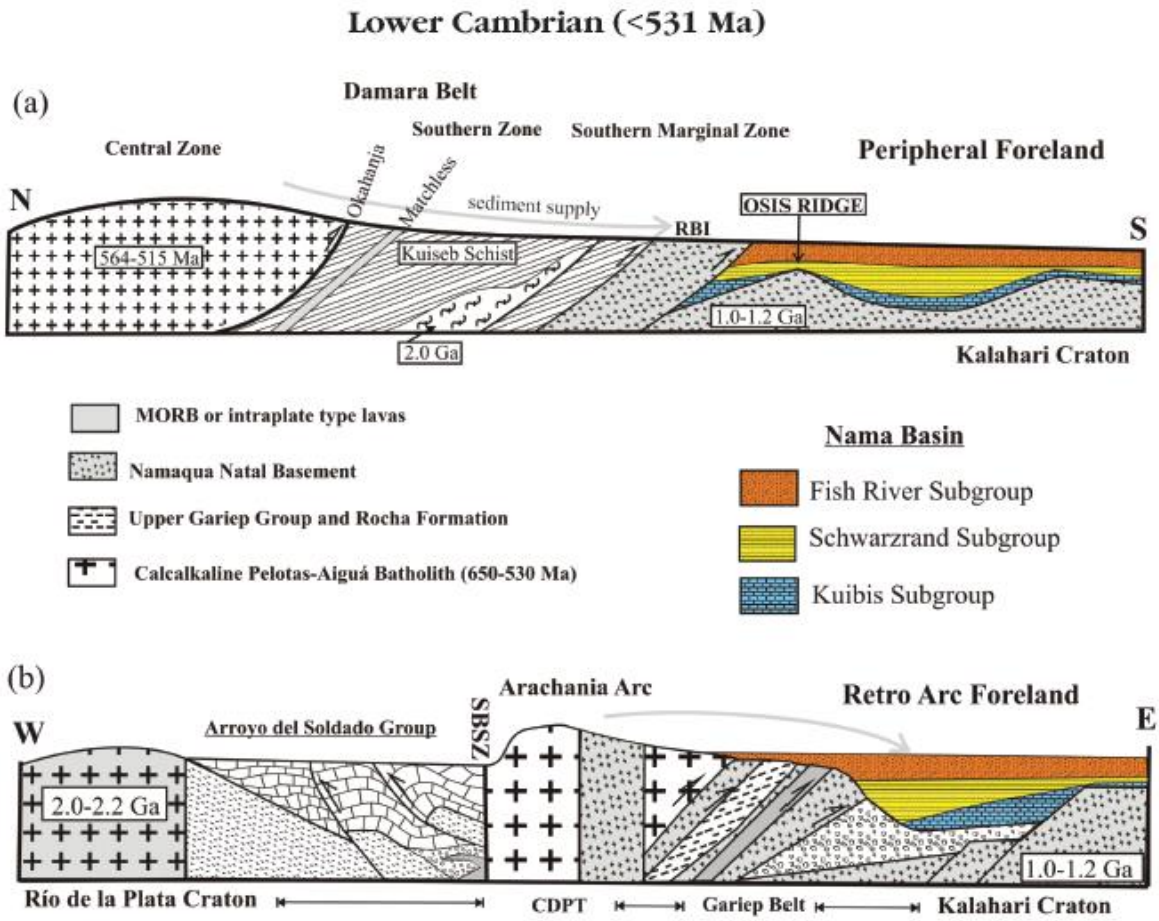

Figure 5: (a) North- South-trending cross section from the Damara Belt in the north to the Nama Basin in the South. (b) Proposed location of the RPC (Río de la Plata Craton) and KC (Kalahari Craton) at 530 Ma based on previous studies ((Blanco, 2010; Blanco et al., 2011; Blanco et al., 2009) from (Blanco et al., 2014).

Once the Khomas Sea closed, the detritus from the active Damara and Gariep continental margins was deposited on the Southern Foreland as distal reddish molasse sediments that form the upper part of Nama Group, namely the Nomtsas Formation and the Fish River Subgroup (Frimmel et al., 2011; Grotzinger et al., 1995). The end of the Damara and Gariep orogenic deformation coincides with the progression from the Schwarzrand to the Fish River Subgroup. Syn-orogenic sequences are represented by the numerous unconformities of the Kuibis and the Schwarzrand (Figure 5). The basal part of the Fish River Subgroup shows stacked angular unconformities that are formed as a response to the multiple thrust and deformation events that took place (Geyer, 2005).

1.6. Lithostratigraphy of the Nama Group

The Nama Group consists of three subgroups (Figure 6) that are from base to top Kuibis, Schwarzrand, and Fish River (Germs, 1983). Here, the rock successions of the Nama Group have an age range from Ediacaran to Cambrian times (Germs, 1995; Meert et al., 1997). Previous stratigraphic correlations suggests that the Nama sedimentary rocks also are present in the Witvlei and Gobais basin (Hegenberger, 1993), as well as in the Vanrhynsdorp region of South Africa, where the Nama Group is equivalent to the Vanrhynsdorp Group (Germs and Gresse, 1991).

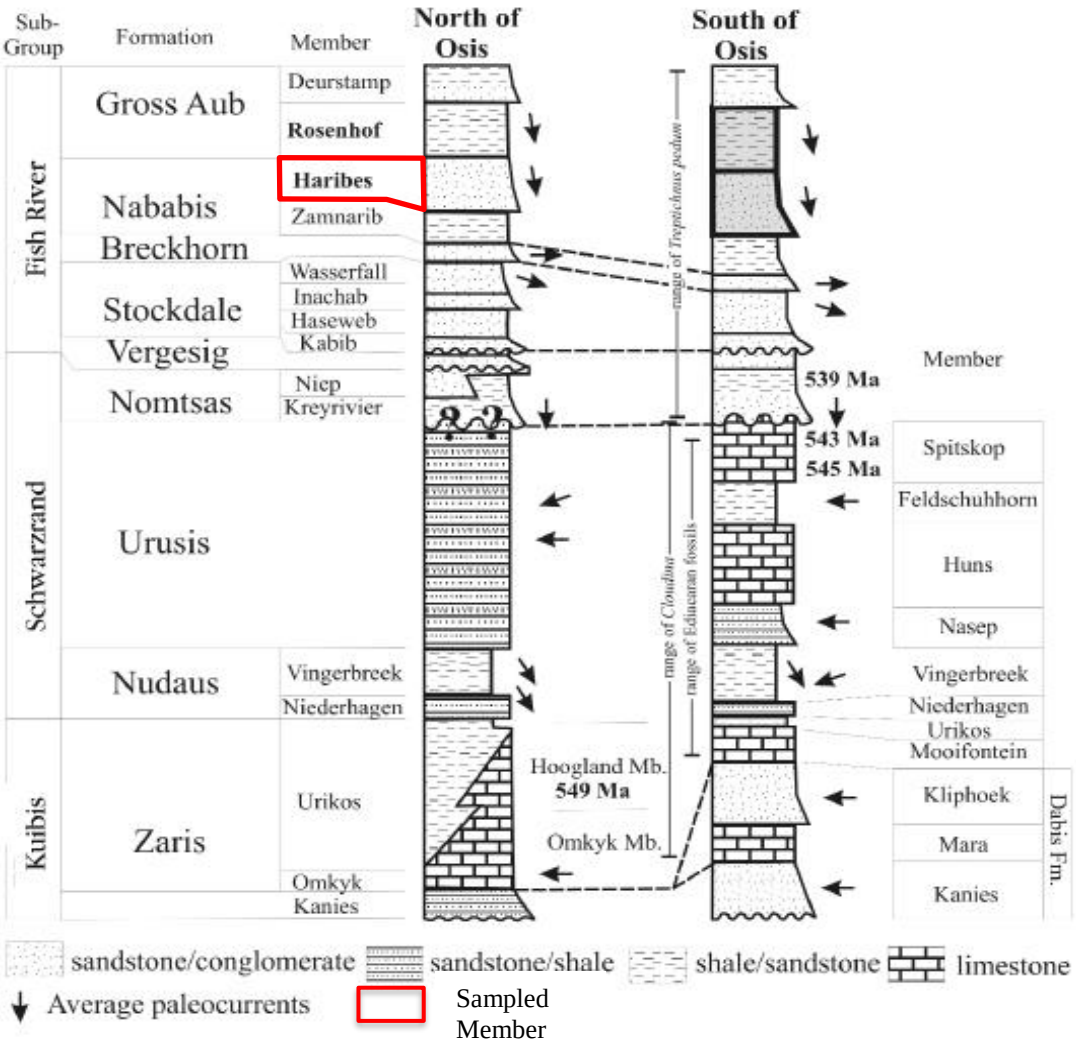

Figure 6: Stratigraphic columns of the Zaris sub-basin (North of Osis Ridge) and Witputs sub-basin (South of Osis Ridge). Suggested paleocurrents of the Nama Group after Germs (1983). Ages represent tuff layers dated by Grotzinger et al., (1995) and paleontological data after Germs (1972). Modified from Blanco et al., (2014).

1.5.1 The Kuibis Subgroup

The pre-Nama relief was flooded by a transgressive sequence represented by the Kuibis Subgroup in which the deposits reflect a shallow marine environment (Geyer, 2005; Meert et al., 1997). One can trace a major unconformity at the base of the subgroup that reaches over 1000 km. Sediments of the Kuibis Subgroup are believed to originate from the Kalahari Craton in the east (Germs et al., 2009). The Osis Ridge divided the Witputs and the Zaris Sub-Basins during Kuibis and the majority of Schwarzrand times. Two cycles can be traced in the Kuibis Subgroup both north and south of the Osis Ridge proximity. The base of each cycle has a pebbly quartzite composition, changing into shale and limestone as one moves stratigraphically upwards, respectively. The second cycle truncates the first cycle towards the Osis Ridge (Germs, 1972, 1983; Germs et al., 2009).

These two cycles can also be found further South of Orange River that divides Namibia and South Africa. Here, the carbonate cycles of the Mara and Mooifontein Members are replaced by two quartz sandstones with shale units that come from the Kamieskroon Ridge. Towards the deeper parts of the Zaris and the Witputs sub-basins (northwest and southwest), the fluvial Kuibis Subgroup sandstones transition into marine shale and limestone. The Kuibis Subgroup that is present in the Zaris sub-basin serve as a northwest-dipping microbial carbonate ramp that is storm-and-wave dominated (Grotzinger et al., 2005; Grotzinger, 2000; Saylor et al., 1998). The carbonate ramp interfingers with shales of the Urikos Member in a northwesterly direction. These shales were deposited offshore in a relatively deep basin. Very little information of the Kuibis Subgroup carbonates in the Witputs sub-basin exist. However, northwesterly trending patch reefs and slump lineaments in shelf lagoonal micrites of the Mooifontein Member may have been formed on topographic highs that are fault controlled (Germs et al., 2009).

1.5.2 The Schwarzrand Subgroup

The deposition of the overlying Schwarzrand Subgroup changed the basin morphology with clear facies changes and differences in sediment accumulation from west to east (Geyer, 2005). It is composed of green-colored clastic sedimentary rocks in the lower part that decrease in maturity and change into a reddish color as one moves stratigraphically upwards to the Nomtsaas Formation. One can also find thick limestone units, e.g. the Huns and Spitskop Members in the Urusis Formation. However, these limestones are only present in the southern part of the Witputs sub-basin (Germs et al., 2009). They pinch out eastwards as well as towards the Osis Ridge in a northward direction.

One can find thrombolites and stromatolites in the Urusis Formation carbonate deposits that are similar to those in the carbonate ramp of Kuibis Subgroup (Grotzinger, 2000). The Kalahari Craton generally supplied the detritus in the Nudaus and Urusis Formation. Although, there is indication of a change in provenance for the basal part of the Nudaus Formation in the northern Zaris sub-basin (Germs et al., 2009). According to Germs (1983), the source was the Damara orogenic belt that already transported sediments during Kuibis times.

1.5.3 The Fish River Subgroup

The transition from the syn-orogenic Schwarzrand Subgroup of Ediacaran age to the late- or post-orogenic Fish River Subgroup of Lower Cambrian age gave rise to a change in deposition. Subsequently, as the Osis Ridge (which derived from the Damara orogen) lost its importance as a major source, facies changed and further development of a peripheral foreland basin on the Kalahari Craton took place. Predominantly, sediment transport that came from the north and west were deposited in a braided fluvial environment (Germs, 1983). Mature shelves that developed were thick uniform sequences of fine- to medium -grained, white and even red to purple silicates. The Fish River Subgroup was therefore deposited in a broadened, yet uniform

basin with a sequence of red clastic of shallow marine and fluvial origin (Geyer, 2005). Molasse sediments that are orogen-derived, onlap a basal unconformity in a craton-ward direction and overstep older sequences in its path (Germs and Gresse, 1991; Gresse and Germs, 1993).

Sediments from a westerly transportation direction indicates that the Fish River has another source other than the Damara event. A depositional signature that is characterized by a synchronous continent – continent collision can be found (Geyer, 2005). This is possibly related to the Gariep Orogeny (Stanistreet et al., 1991). The clastic sediments of the Fish River Subgroup derived from the western Gariep mountain, while the marine belt moved south and southeast (Geyer, 2005). Paleocurrents suggest that the majority of the Stockdale Formation was transported from the north- northwest, followed by the Breckhorn Formation that mainly derived from the west. (Germs, 1974, 1983). The later parts of the Fish River Subgroup (e.g. Zamnarib and Rosenhof members) can be interpreted as a transgressive stage (Geyer, 2005). Thus, a pronounced transport from north to south for late Fish River deposits has been suggested (Germs, 1983).

1.5.3.1. The Tses 1 borehole

According to (Geyer, 2005), the only complete record of the Fish River Subgroup comes from the Tses 1-borehole. The borehole was entirely cored by Aquitaine SWA and De Beers Oil Holdings in 1971 to search for hydrocarbons. It provides a general standard for present day distribution of the Nama Group in terms of lithostratigraphy, thickness and facies development. The borehole is located at 18°04’12’’E and 25°50’30’’S, roughly 59 km NW of outcrop where the samples for this project are collected.

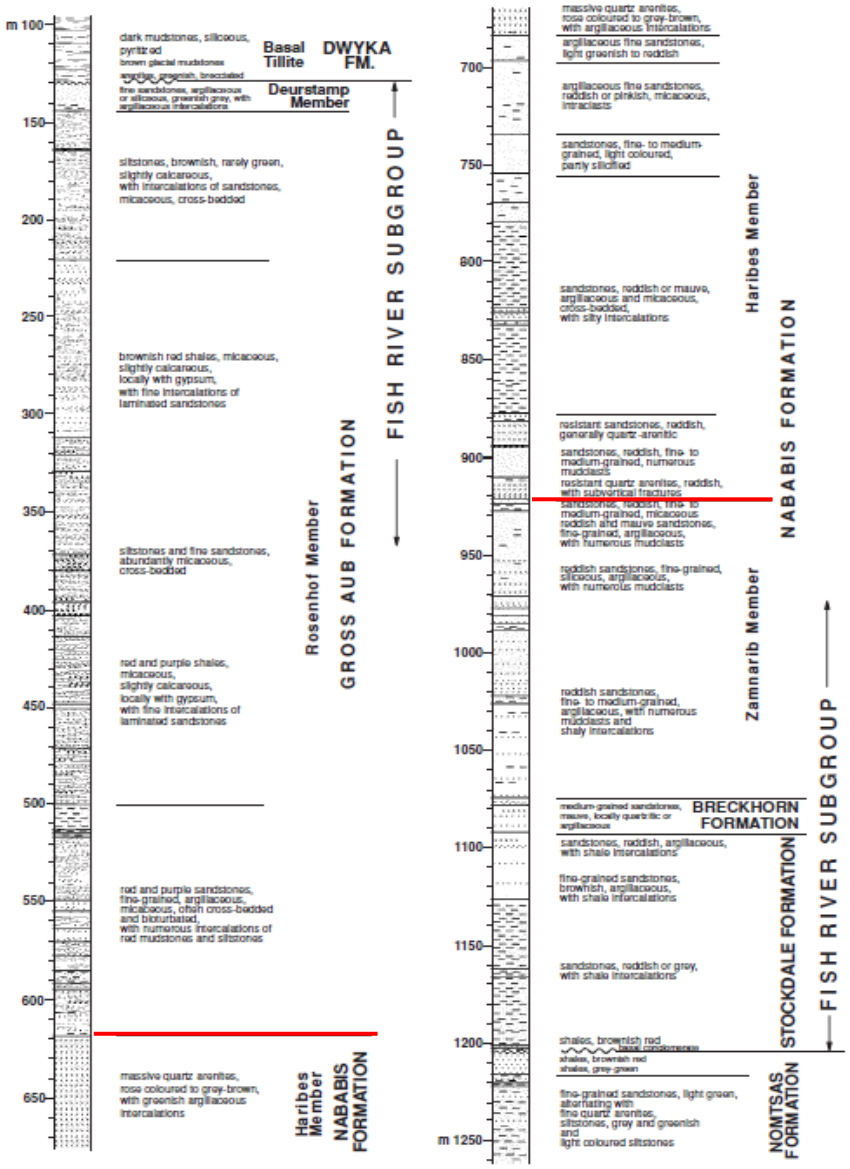

Figure 7: Well profile of Tses 1-borehole, modified after Geyer (2005).

The section of interest in the Tses 1-borehole starts at depth of 617m below surface (Figure 5). This marks the boundary between the Gross Aub Formation (Rosenhof Member) and the Nababis Formation (Haribes Member). Here, one can find termination of a relatively uniform collection of rose-grey to brown-grey quartz arenites (Geyer, 2005). The top unit of the Haribes Member is 66 m thick and consists of thick beds with content of mica flakes followed by abundant flat shale clasts at their bases. One can also find horizontal stratification as well as cross-bedded stratification, the latter more rarely (Geyer, 2005). Below the top unit, one can

find 52 m of sandstones that are pink to purple, argillaceous and micaceous with hints of gypsum and mud clasts. At approximately 735 m depth one can find a 20-m thick section of porous sandstones that are beige in color, packed with black and brown spots similar to what one can find in outcrops (Geyer, 2005).

The largest section of the Haribes Member at Tses 1-borehole contains 122 m of argillaceous and micaceous purple sandstones. Flat shale clasts appear frequently along with horizontal stratification as well as minor observations of low-angle cross-bedding and shale intercalation (Geyer, 2005). Further down the Tses 1-borehole, one can find the basal of the Haribes Member. The 44-m thick resistant unit comprises a 17m-thick upper part of purple quartz-arenitic sandstones, followed by purple, pink and brown medium grained sandstone with several shale clasts. Herringbone cross-stratification can be observed, although cross-stratification is more common. The lower 12 m consist of purple and quartz-arenitic sandstones with argillaceous pebbles. (Geyer, 2005).

1.6. Paleontology

The lower part of the Nama Group is considered as the Kuibis Subgroup in addition to the Nudaus and Urusis Formations of Schwarzrand Subgroup. It contains *Cloudina* and trace fossils that are small, display small diversity and are very scattered (Germs, 1983). The *Cloudina* has for a long time been considered as an index fossil of Ediacaran times (Grant, 1990). Three ash beds of a biozone were dated by U-Pb on zircons between the Zaris Formation (Kuibis Subgroup) and the Urusis Formation (Schwarzrand Subgroup). This zone can generally be regarded as a carbonate biozone, which yields the following radiometric ages; 549 ± 1 Ma, 545 ± 1 Ma and 543 ± 1 Ma, moving stratigraphically upwards (Grotzinger et al., 1995). This coincides well with reported occurrence of the *Cloudina* elsewhere in the world, e.g. the Ara Group in Oman. Here, U-Pb dating on zircons of an ash bed yielded an age of 542.0 ± 0.3 Ma,

which was directly above thrombolytic and stromatolitic framestones containing *Cloudina*. Furthermore, a negative excursion of δ^{13} C down to -5 ‰ PDB was reported, which can be representative of the Precambrian – Cambrian boundary (Amthor et al., 2003). Also, occurrence of the body fossil *Pteridninum Carolinaense* is present. Thus, the Spitskop Member has been assigned to the end of the Ediacaran age (Germs, 1995).

A transition into the Fish River Subgroup of Lower Cambrian age can be recognized by the widespread occurrence of *Trichophycus pedum* along with other trace fossils that are more complex and larger in size than those in the underlying Ediacaran sediments (Buatois et al., 2013). According to Germs (1983), the Haribes Member only contain *Skolithos*, whereas the Rosenhof Member of Fortunian age contains most of the trace fossils in the Fish River Subgroup, namely *Ptrichophycus, Phycodes and Tretichnus (Aceñolaza et al., 2009).* Geyer (2005) considered *Trichophycus pedum* to be produced from an opportunist organism that easily adapted to stressful conditions. It has been reported in intertidal-flat and shallow sub-tidal zones (Geyer and Uchman, 1995) as well as in offshore wave-dominated marine settings (Buatois et al., 2013). One explanation is that a rise in oxygen level sped up the evolution of the metazoan complexity (McFadden et al., 2008; Wood et al., 2015). Subsequently, recordings for the first 10 My of the Cambrian indicates a greater diversity of body plans and skeletal organisations, including stem-group members of *bilaterian pyla* (Knoll, 2003). Suspension feeder and agrichnial farmers supposedly created ichnoassemblages of the Fish River Subgroup (Geyer, 2005).

Table 3: Stratigraphic distribution of fossils, stromatolites and thrombolites of the Nama Group based on work by Germs (1983, 1995; Grotzinger et al., 2000(Wood et al., 2002); Geyer, 2005) (Taken from (Germs et al., 2009).

Sub-group	Stratigraphy		Ediacaran fossils	Skeletal fossils calcified meta-phytes	Trace fossils, biolaminites*	Organic-walled microfossils	Stromatolites thrombolites
	Formation	Member					
Fish River	Gross Aub	Deurstamp Rosenhof			*Trichophycus (Treptichnus) pedum* *Enigmatichnus africani, Gordia Planolites, Paleophycus, Treptichnus pollardi, Trichophycus pedum*		
	Nababis	Haribes			*Skolithos*		
		Zamnarib			*Skolithos, Trichophycus tripleurum*		
	Breckhorn						
	Stockdale	Wasserfall Inachab					
Schwarzrand	Nomtsas	Niep Kreyrivier			*Curvolithos, ?Diplichnites, Neonereites biserialis, N. uniserialis, Trichophycus pedum, T. coronathum*	*Vendotaenia*	
	Urusis	Spitskop	*Pteridinium car. Swartpuntia germsi*	*Cloudina Namacalathus*	*Neonereites uniserialis, Strepthichnus narbonnei*		*Acaciella or Kulparia* thrombolites
		Feldschuh-horn					
		Huns	*Cyclomedusa Nasepia*	*Cloudina* cal. *metaphytes*	*Brooksella, Curvolithos, ?Didymaulichnus*	*Chuaria circul. Leiosphaerids Vendotaenia*	*Acaciella* or *Kulparia Boxonia, Gymnosolen* or *Katavia,* thrombolites
		Nasep	*Paramedusium ?Pteridinium*		*Trichophycus (Treptichnus), Archaeichnium*		
	Nudaus	Vingerbreek	*Pteridinium*				
		Niederhagen	*Pteridinium Rangea*		*Arumberia**		Flat concentric-type stromatolites
Kuibis	Zaris	Urikos Mooifontein		*Cloudina* cal. *metaphytes*		*Bavlinella fav ?Comasphaeri-dium*	*Conophyton*-like stromatolites thrombolites
	Dabis	Kliphoek	*Ernietta, Namalia Orthogonium, Beltanelliformis, Pteridinium, Rangea*		*Bergaueria (Intrites), Buchholzbrunichnus kröneri, ?Skolithos Arumberia**		
		Mara		*Cloudina*			
		Kanies					

Methodology

2.1. Geochemistry preparation

The grains for the XRD were carefully hand milled in an agate beaker down to very fine silt and clay particle size. This was a measure to avoid causing damage to the crystals as well as sample contamination.

2.2. Heavy mineral preparation

A razor blade was used to divide the minerals from a sample into several smaller, equal heaps on a clean sheet of paper. It is usually recommended to use a micro splitter prior to mounting, but this was not available at the UiS. Thus, a more inaccurate approach had to be set in motion. Once satisfied, the minerals were handpicked and mounted on a two-sided tape with guidance through an optical light microscope. These minerals were arranged and lined up nicely in a way that made it easy to find the proper orientation when performing the various analyses. It was therefore important to avoid having too many minerals at one point, as it could be misinterpreted.

Further on, a two component glue was made and casted up to approximately 1 inch in height. This glue was composed of EpoFix Resin and EpoFix Hardener with a 15:2 relation, respectively. The mounds were then left to dry under a separate air ventilation system for 48 hours to make sure they were properly hardened. Once the mounds were completely hardened, the surrounding plastic circles used to cast were cut off.

The mounds were then polished by hand on glass plates humidified by a fluid mixture consisting of silicon carbide powder with different grit sizes and tap water. An optical light microscope was used regularly to check for and avoid grain loss when swapping between grit sizes (320, 600 and 1000). A TegraPol-35 by Struers was then used to perform the very finest polishing

for the mound surface. Two variations were used. The roughest was a DAC-plate of 3 microns, while the second plate, PAN, was 1 micron. By using small synthetic diamonds mixed with tap water one could maintain a wet surface during this process. Each sample were polished for 10 minutes per plate to ensure a clean and transparent mound surface. The mounds were then put in a basket of water and placed in a device that sent shockwaves to remove any impurities from the polishing-phase. Finally, the samples were coated with carbon by using a machine called K550 by Emitech to allow a steady flux and avoid charging. Other viable coating agents are e.g. palladium or gold.

2.3. X-ray diffraction (XRD)

X-ray diffraction (XRD) is a principal method used to characterize crystalline materials such as minerals and determine their structure. The XRD-device has three main components: A sample holder, an X-ray detector and an X-ray tube. By utilizing a crystalline solid's unique and characteristic X-ray pattern, one can identify the phase related to a specific mineral. To produce the X-rays, a metal is used as source. In this project, copper (Cu) was used. It has a wavelength of 1.5418 nm (λ=1.5418). The stacked crystals are considered as repetitive units at spaced intervals (d-spacings) given through $d = \lambda/2$.

Bragg's Law is given:

$$2d\ sin\,\theta = n\,\lambda$$

Where d is d-spacing, θ is Bragg's angle, n is an integer and λ is X-ray wavelength.

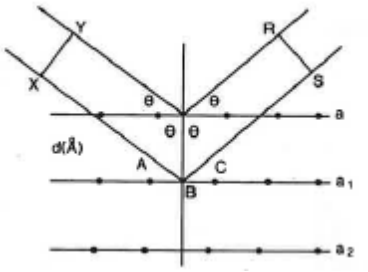

Figure 8: Illustration of Bragg's law (from Hardy and Tucker, 1988). a, a_1, and a_2 are lattice arrays of atoms, regarded as an infinite stack of parallel, equally spaced planes. If a wavewront X-Y is incident on a-a_1 the reflection pat from the lower plane (a_1) is longer, i.e. AB + BC = Δ = difference in paths of wavefronts. (Taken from (Emery and Robinson, 1993)

The generated X-rays are assembled through filters and directed towards the test sample. By rotating the sample, one can collect the intensity of the reflected X-rays. The range was set from 4° to 70° in this project. Constructive interference appears when the direction of incident-angle of the X-rays reach a desired angle from Bragg's Equation. The peaks obtained were then cross-matched with a database library built in the XRD-Software called Diffrac.Suite, which is produced by Bruker to determine minerals as seen in the example of Figure 6.

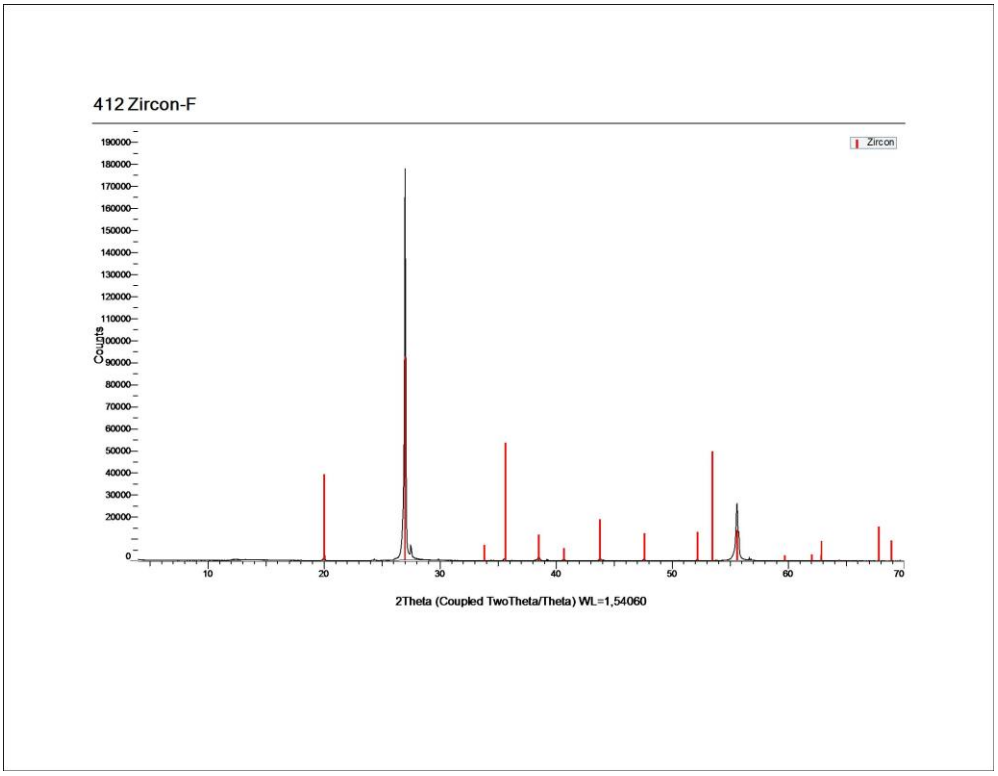

Figure 9: Example from the XRD analysis. The zircon fraction of sample 412 displaying peaks of zircon.

2.4. Field Emission Gun Scanning Electron Microscope (FEG-SEM)

The field emission gun scanning electron microscope used for this thesis was the model Supra 35 VP (Figure 5) and SmartSEM software made by Zeiss. A strong beam of electrons is generated from an electric gun to scan the mounds. Electrons are narrowed down and concentrated to 5 nm when the electron stream passes through lenses. The aperture size is the size of the opening where electrons phases. Generally, this was set to 30 µm, expect for the zircon concentration mounds that were mapped in CL where it was set to 300 µm to optimize the signal from the samples. Another attribute is the specific voltage, EHT, of the electrons that set between 15kV and 20kV.

Several types of energy signals are produced and/or reflected when the electron beam hits the surface sample. These are collected by the four different detectors that are installed to the device, which in this project are light (Cathodoluminescence, CL), Secondary Electrons (SE), Back-Scattered Electrons (BSE) and X-Rays (Energy Dispersive System, EDS). Below (Figure 6), one can see a schematic drawing of a general SEM/EDX system after Beck (1977).

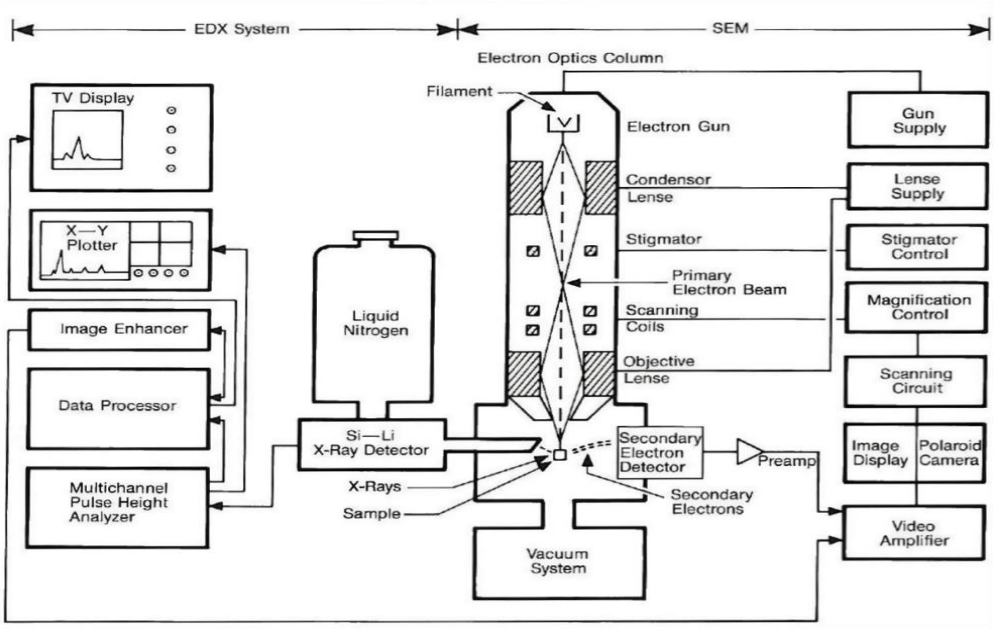

Figure 10: Schematic drawing of SEM/EDX system (Beck, 1977)

When minerals are bombarded with high energy, emitted photons of a characteristic wavelength occur (Egerton, 2005). These wavelengths are in the visible spectrum and are picked up by the Cl-detector. This is a very useful method to be used on luminescent minerals such as zircons, as it displays the internal structure of the crystals in terms of cores and zones (Figure 8). It is worth noticing that the quality of the CL image may vary depending on if the material is phosphorescent or fluorescent. The fluorescent mineral immediately re-emit absorbed radiation, whereas the phosphorescent will re-emit at a later stage.

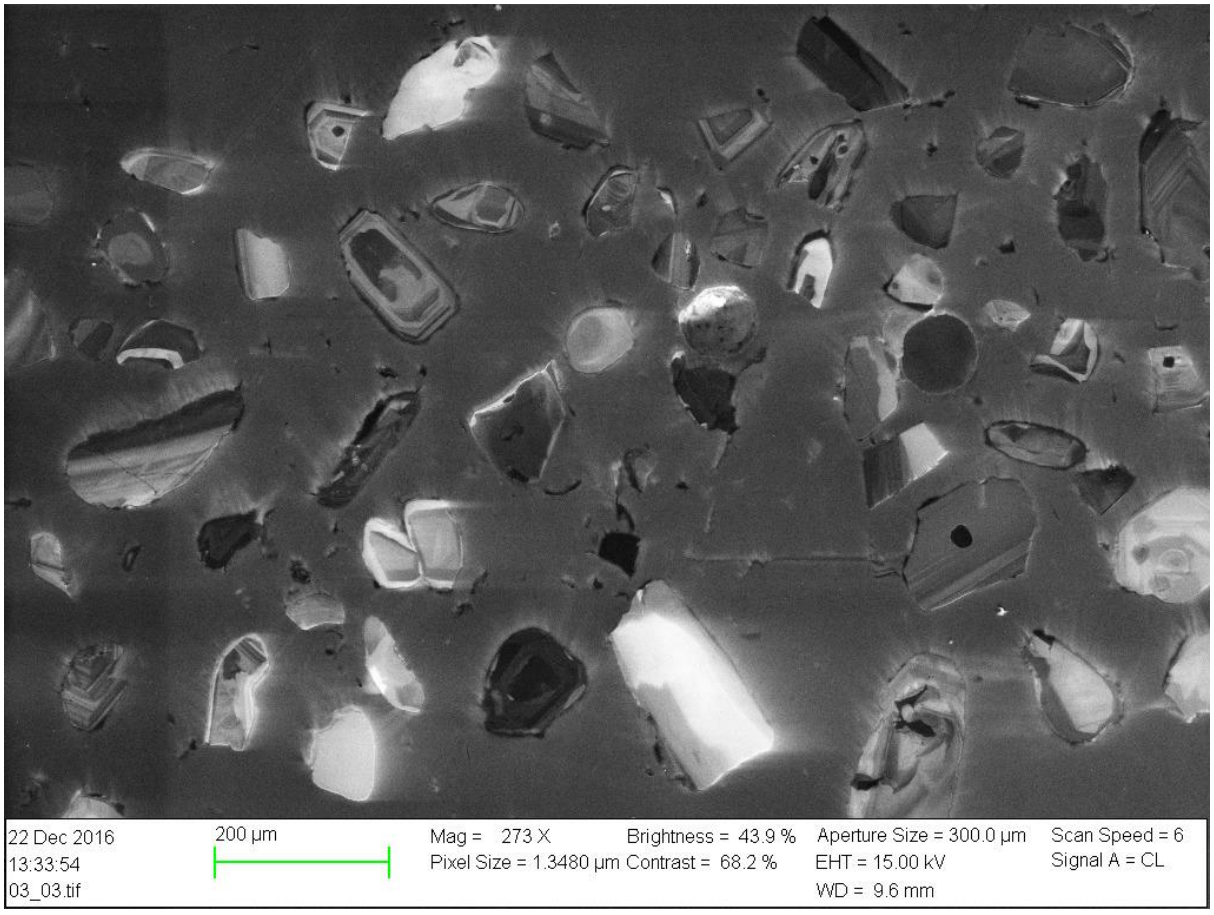

Figure 11: CL-image of a zircon mound where one can see the zonation of the zircons diving rim from core.

Secondary electrons are gathered in a SE-detector. They are useful to image the surface of the sample through a scanning sequence to create SEM-micrographs. The detector e.g. be used in the initial phase to find the orientation of the studied sample and to adjust focus of the imaged surface. Generally, the emission of the secondary electrons is influenced by morphology and

topography of the sample mounds. As primary electrons strike with great energy on the surface in a system that is pre-pumped to vacuum state, electrons are emitted from an inner shell of an atom. The depth of surface penetration depends on mineral composition, quality of the sample and the level of voltage. I.e. electrons in a system set to 20kV should penetrate further than one of 15kV. Another important feature of the SEM is the BSE, backscattered electron detector. This detector operates mainly by observing the reflected, or backscattered, primary electrons, which are a result of elastic scattering from the atoms solid due to the electron beam. The back scattered electrons can change direction, but their energy level is mostly conserved. This allows electrons from deeper into the sample to be emitted and detected in contrast to the secondary electrons, which behave inelastic. The high energy level of the back scattered electrons unlocks the ability to map elements on the surface. When displayed on a screen one will notice differences in contrast depending of an element's atomic number in the periodic table. I.e. an element with a low atomic number will emit fewer electrons and thus be dark-colored. An element with a high atomic number, however, will appear as bright-colored due to more emitted electrons.

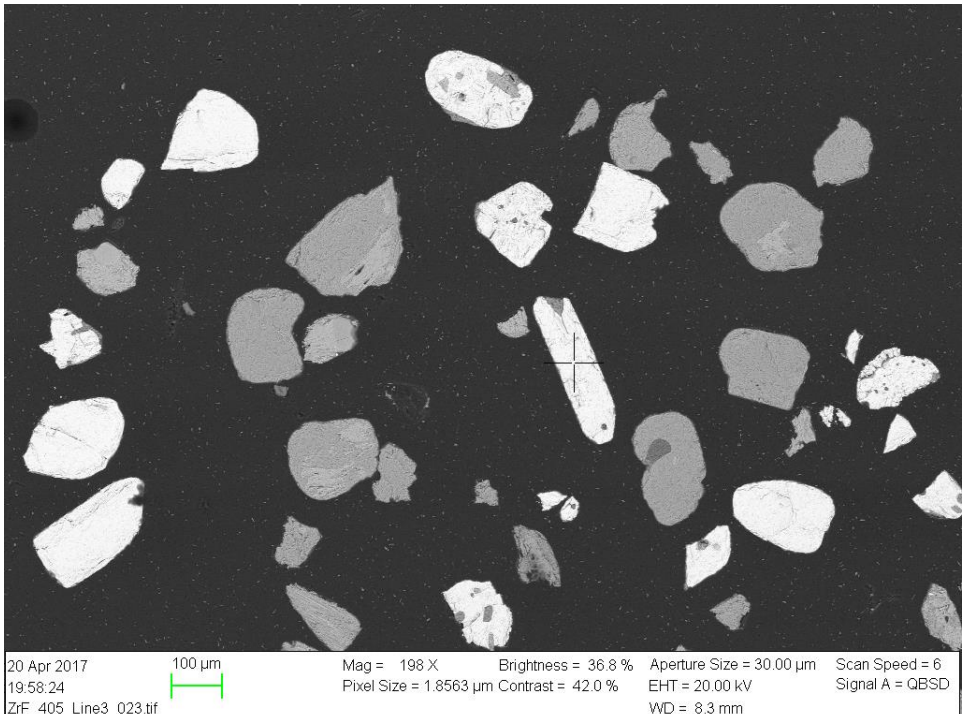

Figure 12: Illustrating greyscale differences. The cross marks a bright colored zircon grain due to higher atomic number relative to the dark colored quartz region above the cross

The interactions on atomic level that are mentioned in the paragraphs above will also cause X-rays to be emitted. These signals are collected by the Energy Dispersive Spectroscopy (EDS) detector. The Energy Dispersive X-ray Spectroscopy System delivered by EDAX, processes the data in the EDAX Genesis Software. This system analyses the chemical composition of either a point defined in the software or a larger scanned area. The energy level of the discharged X-ray from each element will contrast due to the difference in atomic structure of various elements. A spectrum of the present elements is created that reflects X-rays identified by a silicon crystal saturated with lithium. Here, one can also perform semi-quantification of the weight (wt.%) and atomic weight (at.%). One should keep in mind that the accuracy of the measurements varies on several factors from day to day basis. To minimize the inaccuracy, it is suggested to use standards depending on which minerals that are studied. Optimal attributes were obtained from previous studies on the validity of EDS in analysis by using FEG-SEM (Bekkum and Egeland, 2016).

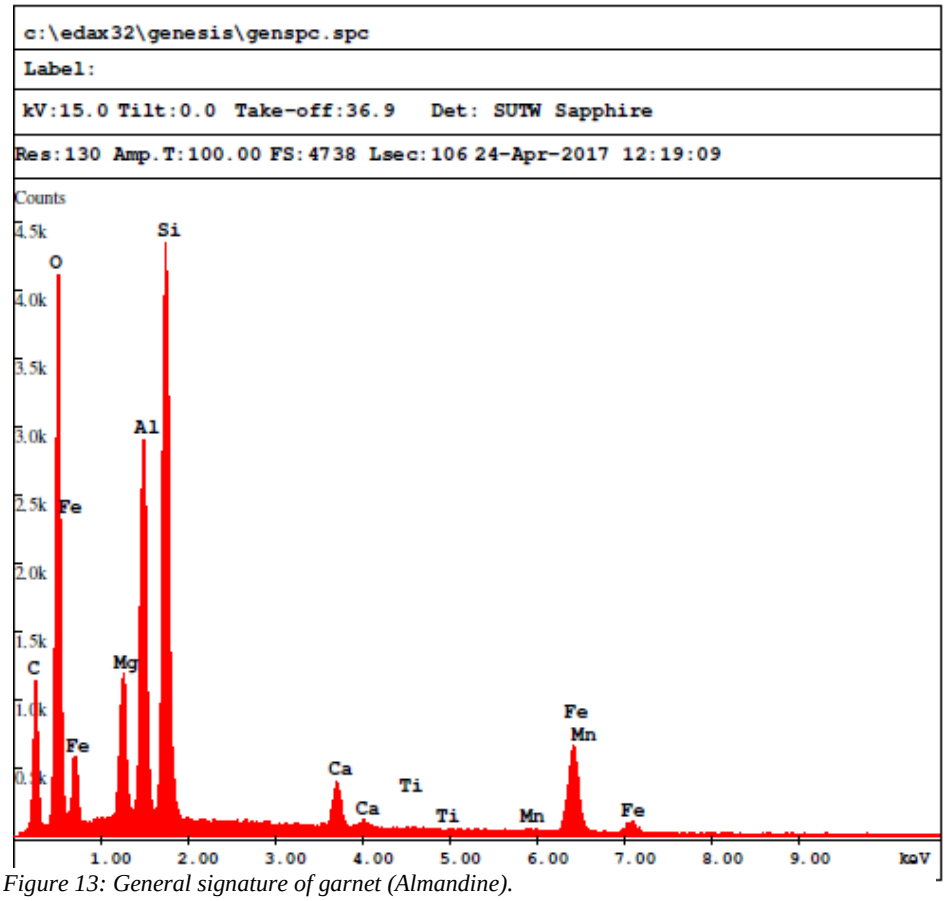

Figure 13: General signature of garnet (Almandine).

2.5. Mineral liberation analyzer (MLA)

MLA is a semi-quantitative measurement that combines imaging by SEM-BSE analysis and chemistry from X-ray mineral identification by EDS. The preliminary analyses were performed at Technische Universität Bergakademie Freiberg (TU Bergakademie Freiberg) in Germany. The devices used were a FEI Quanta 600 FE-SEM together with an EDS system (6130 XFlash EDS) from Bruker. MLA Mineral Editor 3.1 was combined with MLA Mineral Reference editor 3.1 to edit and identify scanned minerals. The results presented later in this thesis were then compiled in MLA Dataviewer 3.1 at UiS, Norway. Finally, the images and analysis were acquired at a working distance of 12mm and an acceleration voltage of 25 kV.

Initially, a quick scan is run to get an overview of the minerals that are present in the sample. Each spectrum is added to a database to a database and is given a color code according to the classified mineral type. Every selected mineral is then setup to be associated to the average value of the respective BSE image. The number of backscattered electrons from a sample coincides with the average atomic number a mineral phase, thus a unique greyscale-value (although minor variations are accepted) can be given to each mineral (Fandrich et al., 2007). Calibration of the greyscale values are performed with gold, silver, copper and quartz standards to ensure good measurements. The BSE-images collected should then correspond to collected EDS-spectrum stored in the database library, thus, mapping on a larger scale can be conducted.

High-resolution scans are done with the use of a BSE-detector. Subsequently, a filter for minimum BSE greyscale level is applied in the process of particulation to remove anything below a given limit. This will remove any impurities i.e. air bubbles, dust and epoxy resin from the mounting process. The next operation is segmentation identify all distinct mineral grains and phases. It outlines regions of homogeneous greyscale levels found in the respective BSE images based on the mineral's average atomic number (AAN) (Fandrich et al., 2007)

MLA offers many measurement modes whereas in this project, grain-based X-ray mapping (GXMAP) is used. This mode operates with a pre-defined grid where identification of particles through BSE images are combined with X-ray spectra with given characteristics. A BSE trigger or a specific X-ray standard trigger is set to ensure high resolution mapping of grains of interest. The data collected is then compared to the mineral database and given a color code according to mineral type. Mixed spectra may occur as unknown minerals if the step-size of the scan is higher than an intrusion. In that case, a script is made to change unknown minerals to a certain point into host mineral for practical purposes.

Results

3.1. XRD analysis

The following figures (14-17) displays the preliminary results for the XRD analysis of the magnetic fractions. A complete overview of the respective zircon and apatite fractions can be found in Appendix D. All magnetic fractions display the nesosilicates; titanite, almandine and grossular with significant peaks. Furthermore, presence of spinel, ulvospinel and magnetite belonging to the spinel group were detected. The XRD also revealed small peaks of gedrite, hematite, chamosite and epidote. Moreover, fluorapatite, rutile and quartz can be identified.

In addition to the general composition of the magnetic fractions carried out by XRD analysis, Mf 412 (Figure 14) also contain traces of diopside of the pyroxene group. Furthermore, Mf 405 (Figure 17) display barroisite of the amphibole group in addition to the clinochlore of the chlorite group.

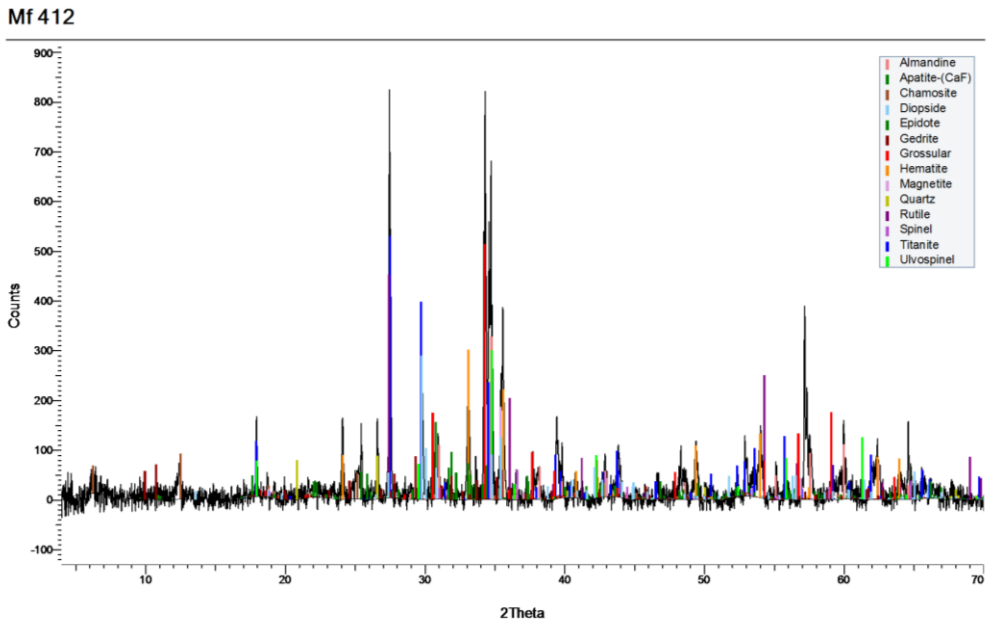

Figure 14: XRD analysis of sample 412 displaying the magnetic fraction composition.

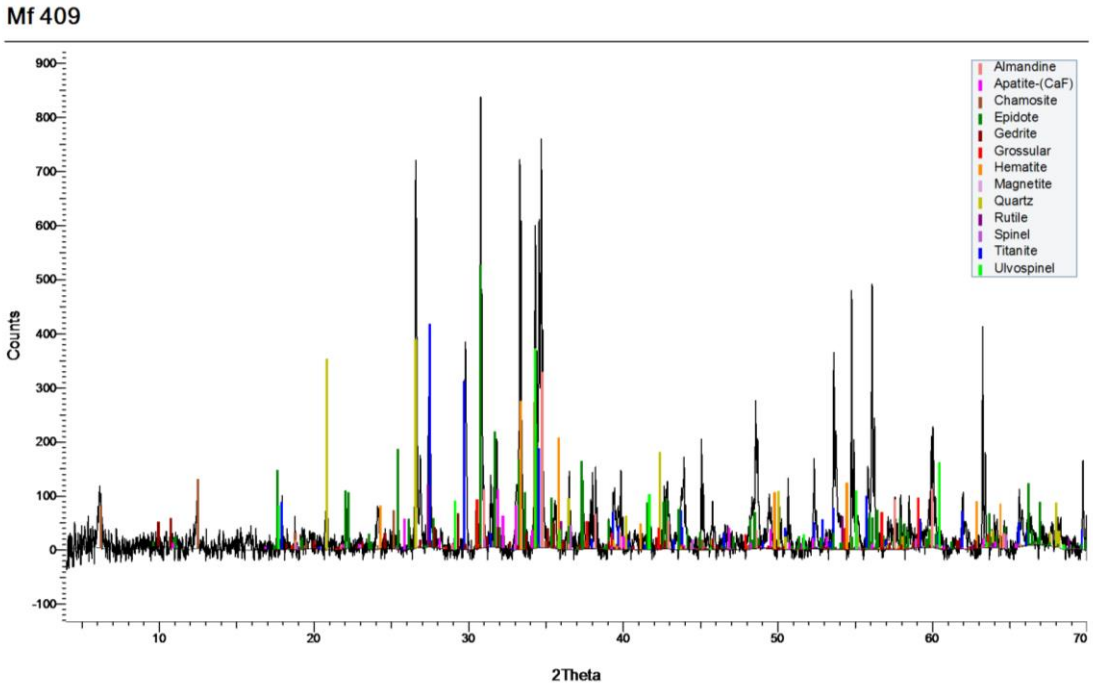

Figure 16: XRD analysis of sample 409 displaying the magnetic fraction composition.

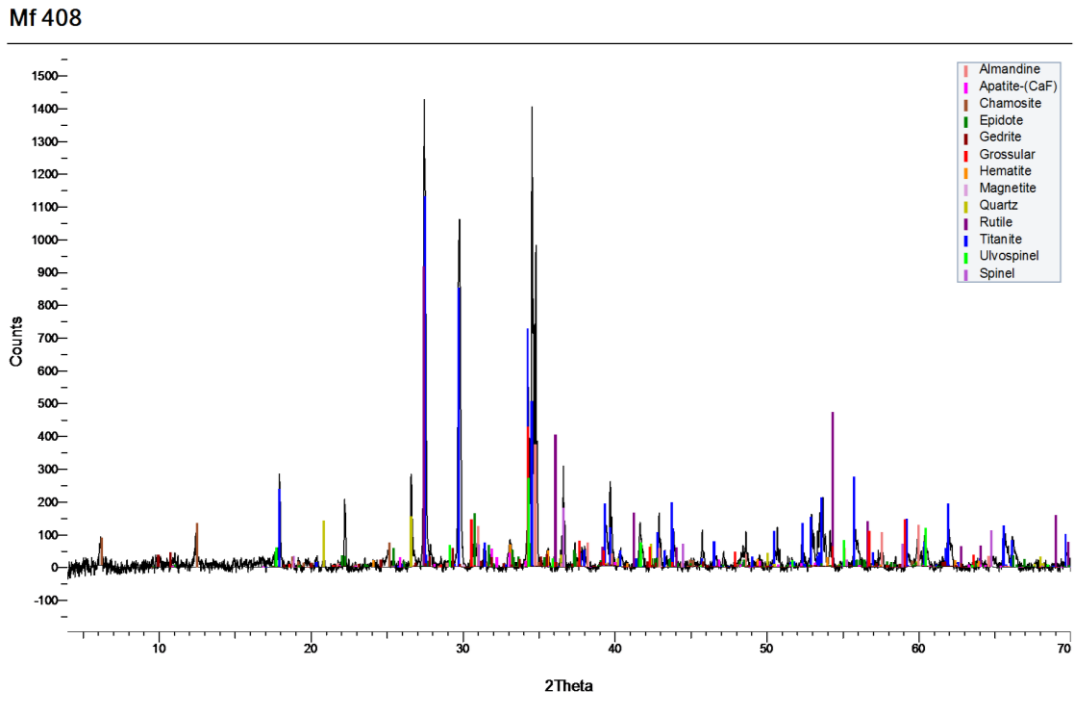

Figure 15: XRD analysis of sample 408 displaying the magnetic fraction composition.

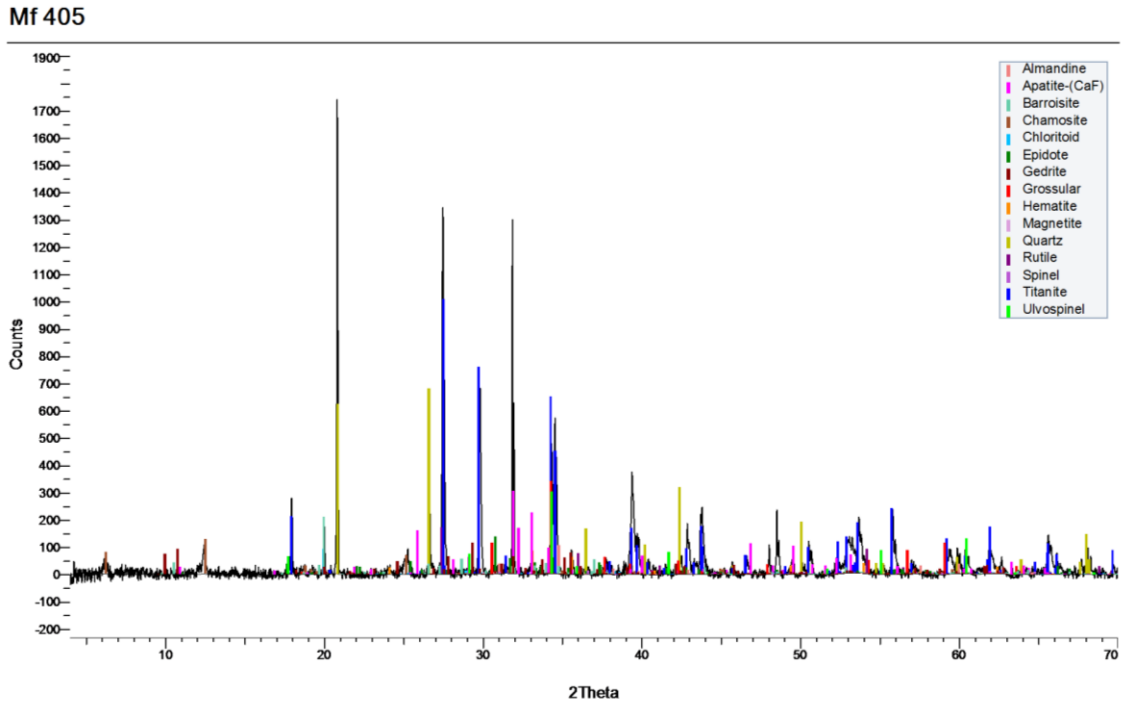

Figure 17: XRD analysis of sample 405 displaying the magnetic fraction composition

3.2. FEG-SEM analysis

Semi-quantification of the magnetic fractions (Mf), apatite fractions (Af) and zircon fractions (Zf) from the Haribes Member of the Nababis Formation for the respective samples can be found in table 4. All samples are analyzed in BSE conditions and the semi-quantitative chemistry has been measured by EDS. The major content of magnetic fractions constitutes of garnet, titanite and ulvospinel with minor occurrences of quartz, rutile, ilmenite, monazite, jadeite, stilpnomelane, tourmaline, barite, apatite, calcite, amphibole and zircon. Moreover, the apatite fractions are mostly made up of Apatite (fluorapatite) and less abundant minerals such as amphibole, feldspar, garnet, magnetite, quartz, rutile, stilpnomelane, titanite and zircon. Finally, the zircon fractions constitute of titanite and zircon, with minor occurrences of amphibole, apatite, feldspar, chamosite, quartz, rutile, stilpnomelane and ulvospinel.

Table 4: Semi-quantification and mineral distribution of magnetic fraction (MF), apatite fraction (Af) and Zircon fraction (Zf) for the respective samples from FEG-SEM analysis.

Fraction type	Magnetic fraction (Mf)				Apatite fraction (Af)				Zircon fraction (Zf)			
Sample	412	409	408	405	412	409	408	405	412	409	408	405
n, grain measurements	126	141	131	146	107	128	109	102	114	116	120	104
Amphibole (Gedrite)	3%	5%	5%	2%	2%	11%	7%		2%	2%	2%	1%
Apatite		2%	5%	3%	89%	75%	79%	96%	1%	3%	1%	3%
Barrite				3%								
Chamosite			5%	1%						1%		
Feldspar (orthoclase)	1%		1%	1%	1%	2%	1%			2%	1%	2%
Garnet (Almandine)	27%	28%	8%	10%	2%							
Garnet (Grossular)	1%	8%	8%									
Ilmenite			1%	1%								
Iron-oxide (Magnetite)	9%	3%	5%	4%		1%	1%					
Monazite		1%										
Pyroxene (Jadeite)		1%	2%	3%								
Quartz	7%	12%	8%	10%	3%	2%	6%		7%	7%	8%	3%
Rutile	2%				2%			1%	10%	3%	9%	9%
Stilpnomelane		5%	2%	1%		8%			1%	2%	2%	
Titanite	27%	21%	48%	51%	1%	1%	5%	2%	25%	54%	40%	35%
Tourmaline		1%		2%								
Ulvospinel	21%	9%		6%						2%		
Zircon	2%	6%	2%	3%	1%	1%	2%	1%	54%	25%	37%	48%
Total	**100%**	**100%**	**100%**	**100%**	**100%**	**100%**	**100%**	**100%**	**100%**	**100%**	**100%**	**100%**

3.3. MLA analysis

From the FEG-SEM and MLA analysis, one can generally find the same minerals in all four samples for all the different fractions. The semi-quantitative analysis performed using the FEG-SEM-BSE-EDS seems to compare relatively well to the semi-quantitative analysis carried out using MLA scans. Although difficult to determine, amphiboles from the SEM could be gedrites, which is associated metamorphism. The MLA could not distinguish between F-, Cl- and OH-apatite, although the SEM could, these have therefore been assembled as apatite. Moreover, Ti-rich magnetite from the SEM analysis was identified as ulvospinel. Similar variations were found in the MLA analysis, although here, it was grouped as magnetite. The MLA analysis did, however, identify less abundant minerals such as yoderite, chromite and spessartine, which the SEM did not.

Another mineral pair that require additional attention is hematite and magnetite. These iron oxides typically only differ in Fe content by 2.5 wt.% based on EDX analysis (Sylvester, 2012) and their greyscale values in BSE are very similar (Figueroa et al., 2012; Shaffer, 2009). Garnets, epidotes and amphiboles can easily be misinterpreted as one or the other as they can be difficult to differentiate.

The minerals in table 5 are based on MLA analysis and can be arranged in groups inspired by Stronz classification. In this project, nesosilicates include findings of yoderite, almandine, grossular, spessartine, titanite and zircon. The framework silicate group is made up of quartz, albite and orthoclase. Furthermore, inosilicates comprise amphiboles. Phyllosilicates include the sheet silicates chamosite and muscovite. Moreover, cyclosilicates includes the ring silicate tourmaline. In addition to the silicates, there are oxides that consist of magnetite, rutile, ilmenite and chromite. One can also find barite of the sulfate group as well as apatite and monazite of the phosphate group. The only carbonate found is calcite. Others are undefined minerals, impurities and bad readings that can generally be disregarded.

Table 5: Mineral groups based on Stronz classification from MLA analysis in Wt%.

Sample / Mineral	Mf 412	Mf 409	Mf 408	Mf 405	Af 412	Af 409	Af 408	Af 405	Zf 412	Zf 409	Zf 408	Zf 405
Nesosilicates	62.87	79.59	86.76	83.54	1.76	3.27	2.33	1.50	80.47	84.19	84.84	73.86
Framework silicates	1.08	4.93	2.94	5.95	2.52	1.26	0.98	0.78	0.46	1.69	1.45	1.05
Inosilicates	2.99	3.27	0.74	0.83	0.02	0.01	0.01	0.03	0.01	0.01	0.00	0.02
Phyllosilicates	1.59	2.03	1.31	2.38	0.10	0.41	0.19	0.09	0.12	0.74	0.41	0.22
Cyclosilicates	0.00	0.10	0.21	0.02	0.00	0.01	0.01	0.00	0.01	0.01	0.04	0.00
Oxide group	30.19	7.78	6.03	5.13	0.11	0.02	0.01	0.70	18.72	9.06	9.81	24.23
Sulfate group	0.00	0.00	0.00	0.29	0.00	0.00	0.00	0.03	0.00	0.00	0.00	0.02
Phosphate group	1.23	2.26	1.96	1.46	95.49	95.00	96.46	96.86	0.22	4.29	3.45	0.60
Carbonate group	0.04	0.00	0.02	0.40	0.00	0.01	0.01	0.01	0.00	0.01	0.00	0.00
Others	0.00	0.03	0.02	0.02	0.00	0.00	0.00	0.00	0.00	0.00	0.00	0.00
Total	100.00	100.00	100.00	100.00	100.00	100.00	100.00	100.00	100.00	100.00	100.00	100.00

3.3.2 Heavy mineral fraction

The magnetic fraction Mf 412 is dominated by almandine (33,15%), magnetite (28,24%) and titanite (27,78%). Less abundant minerals are amphibole, chamosite, rutile, zircon and apatite. Spessartine and ilmenite occur as minor traces. The corresponding apatite fraction Ap 412 is mainly comprised of apatite (98,00%) and titanite (1,23%). Grossular, amphibole, chamosite, and zircon are sparse. Moreover, the zircon fraction Zf 412 display a greater number of zircon (55,35%), titanite (24,92%) and rutile (18,81%), whereas almandine, tourmaline, chamosite and apatite appear only sporadically (Table 6).

Further on, the magnetic fraction Mf 409 is generally composed of almandine (39,92%), titanite (29,49%) and grossular (14,58%). Other substantial minerals are magnetite. amphibole apatite and chamosite. Spessartine, ilmenite, tourmaline, rutile and zircon appear in meager amounts. The apatite fraction Ap 409 is dominated by apatite (96,38%) and titanite (2,62%). Additionally, traces of grossular, magnetite, tourmaline, amphibole and zircon can also be found. The corresponding zircon fraction Zf 409 is comprised of zircon (55,35%), titanite (24,92%) and rutile (18,81%). It also has input of apatite, chamosite, amphibole and tourmaline.

The magnetic fraction Mf 408 is dominated by titanite (63,95%), almandine (13,44%) and grossular (11,91%). Less abundant minerals are magnetite, rutile, chamosite, amphibole and apatite. Spessartine, ilmenite, tourmaline, rutile and zircon appear as traces. The corresponding apatite fraction (Ap 409) is mainly composed of apatite (97,60%) and titanite (1,89%). Almandine, grossular, magnetite, tourmaline, amphibole, chamosite and zircon are sparse. Zf 408 has a substantial amount of titanite (74,76%) and zircon (10,21%) and rutile (9,95%). It is also comprised of small amounts of almandine, grossular, spessartine, magnetite, tourmaline, chamosite and apatite.

Finally, the magnetic fraction of sample 405 constitutes of titanite (72,42%) and magnetite (12,84%). Less abundant minerals are grossular, magnetite, chamosite, rutile, zircon and apatite. Traces of spessartine, barite, ilmenite, tourmaline and amphibole can also be found. The complementary apatite fraction (Ap 405) is mainly composed of apatite (97,64%) and titanite (1,14%). Almandine, grossular, magnetite, barite, amphibole, chamosite, rutile and zircon are sparse. The zircon fraction, Zf 405, has large portions of titanite (46,93%), rutile (24,46%) and zircon (27,12%). Small amounts of almandine, spessartine, magnetite, barite, ilmenite, amphibole, chamosite and apatite are also detected.

Table 6: Minerals identified with MLA. The values are calculated as Wt% of heavy minerals, thus minerals with densities < 2.9g/cm^3 are not included in this table. Additionally; chromite, yoderite and monazite are excluded due to inadequate values ~ 0 Wt%. Different mineral varieties (i.e. Titanite and Titanite-Fe) are grouped as one. A complete table of all the findings can be seen in appendix B.

		Magnetic fractions				Apatite Fractions				Zircon fractions			
Color	Mineral	Mf 412	Mf 409	Mf 408	Mf 405	Ap 412	Ap 409	Ap 408	Ap 405	Zf 412	Zf 409	Zf 408	Zf 405
	Almandine	33.15	39.92	13.44	12.84	0.55	0.65	0.36	0.33	0.58	1.39	1.37	0.60
	Grossular	1.23	14.58	11.91	2.08	0.01	0.02	0.07	0.02	0.00	0.02	0.03	0.00
	Spessartine	0.20	0.35	0.01	0.11	0.00	0.00	0.00	0.00	0.00	0.00	0.01	0.01
	Magnetite	28.24	7.17	3.25	4.08	0.00	0.02	0.01	0.04	0.00	0.03	0.04	0.02
	Titanite	27.78	29.49	63.95	72.42	1.23	2.62	1.89	1.14	24.92	65.23	74.76	46.93
	Barite	0.00	0.00	0.00	0.31	0.00	0.00	0.00	0.03	0.00	0.00	0.00	0.02
	Ilmenite	0.17	0.22	0.09	0.07	0.00	0.00	0.00	0.00	0.00	0.01	0.00	0.01
	Tourmaline	0.00	0.11	0.22	0.02	0.00	0.01	0.01	0.00	0.01	0.01	0.04	0.00
	Amphibole	3.03	3.47	0.77	0.89	0.02	0.01	0.01	0.03	0.01	0.01	0.00	0.02
	Chamosite	1.55	1.13	0.47	2.31	0.07	0.26	0.02	0.09	0.11	0.12	0.07	0.21
	Rutile	2.13	0.89	2.94	1.34	0.11	0.00	0.00	0.66	18.81	9.23	9.95	24.46
	Zircon	1.27	0.27	0.92	1.97	0.02	0.03	0.03	0.03	55.35	19.55	10.21	27.12
	Apatite	1.25	2.40	2.04	1.56	98.00	96.38	97.60	97.64	0.22	4.39	3.52	0.60
	Total	100.00	100	100	100	100	100	100	100	100	100	100	100

3.3.3 Particle size distribution

The following three figures (Figure 18-20) show graphs of particle size distribution for the magnetic-, apatite- and zircon fractions, respectively. From figure 18, it is evident that Mf 405 generally have a higher Wt% of larger particles compared to the other samples. Although, the trend is generally the same. From Figure 19, it is noticeable that Af 412 has the highest Wt% of larger particles, though the trend is similar. The zircon fractions (Figure 20), however, Zf 409 demonstrate a bimodal distribution with smaller particle sizes when compared to the others.

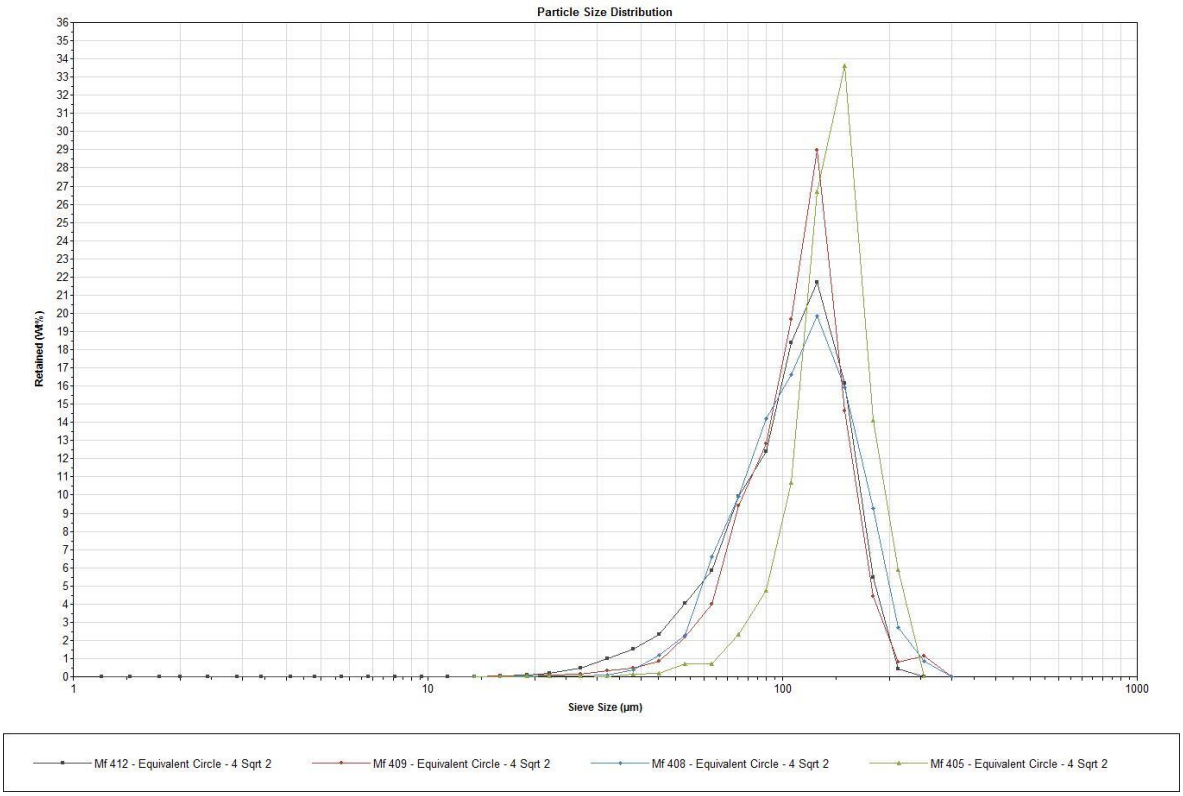

Figure 18: Particle Size Distribution based on MLA analysis of the magnetic fractions (Mf) in microns.

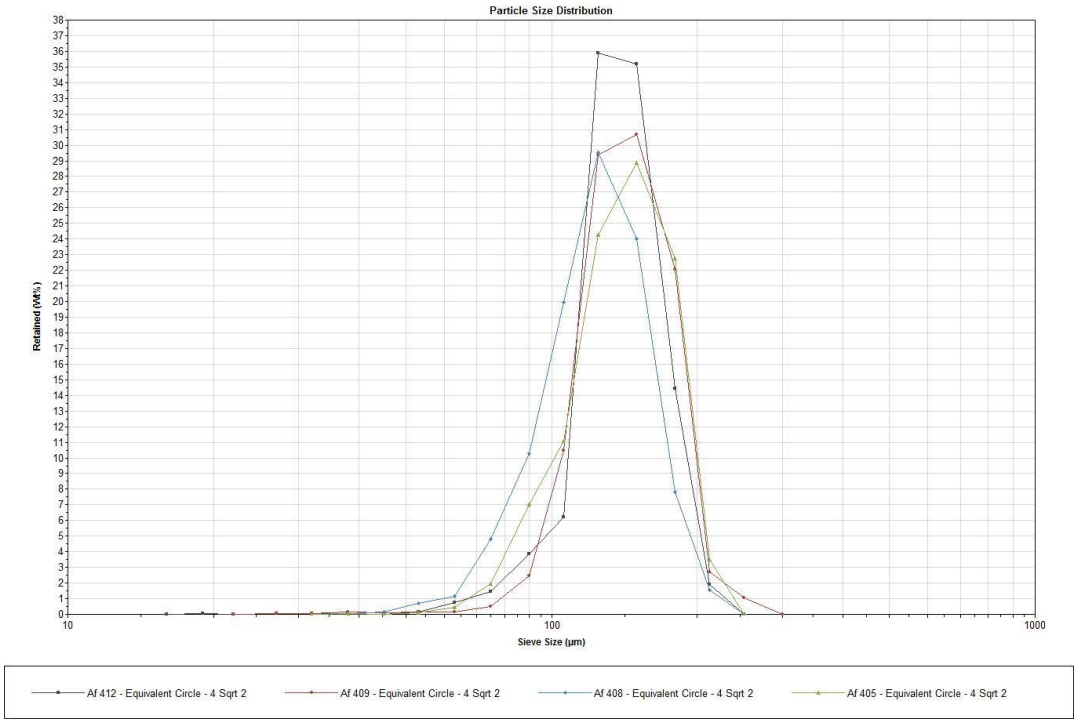

Figure 19: Particle Size Distribution based on MLA analysis of the apatite fractions (Af) in microns.

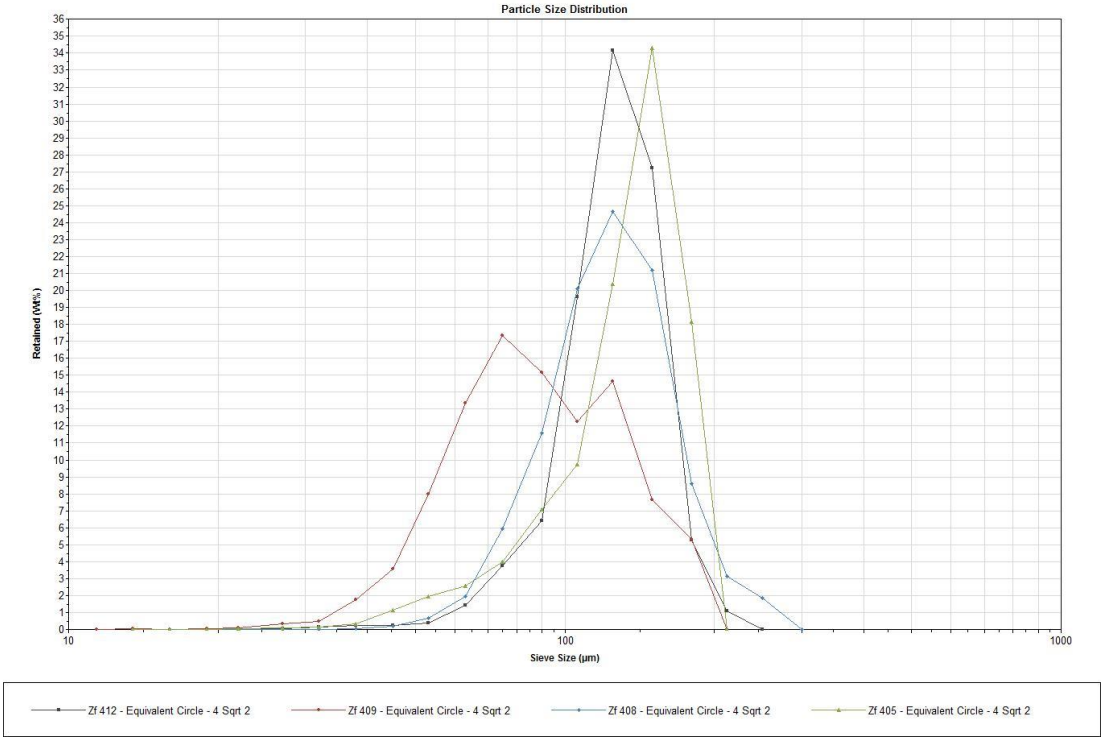

Figure 20: Particle Size Distribution based on MLA analysis of the zircon fractions (Zf) in microns.

Interpretation

4.1. FEG-SEM/MLA

Generally, the SEM and MLA results show similar trends between the different samples (figures 21-22). The main trend shows a larger percentage of iron oxide in sample 412 compared to the others, and a larger percentage of garnets in sample 409. The density and the distribution of garnets vs. iron oxides suggest a change in energy. Garnets are replaced by titanite when moving from sample 412 and 409 to sample 408 and 405. The apatite fractions for the respective samples show no noteworthy change (Figure 23). However, a similar trend as seen in the magnetic fractions is also found in the zircon fractions (Figure 24). An abrupt decrease in zircon and rutile content is recognized and replaced by titanite when moving from sample 412 to e.g. sample 409 and 408. The zircon and rutile content increases in sample 405, relative to sample 409 and 408.

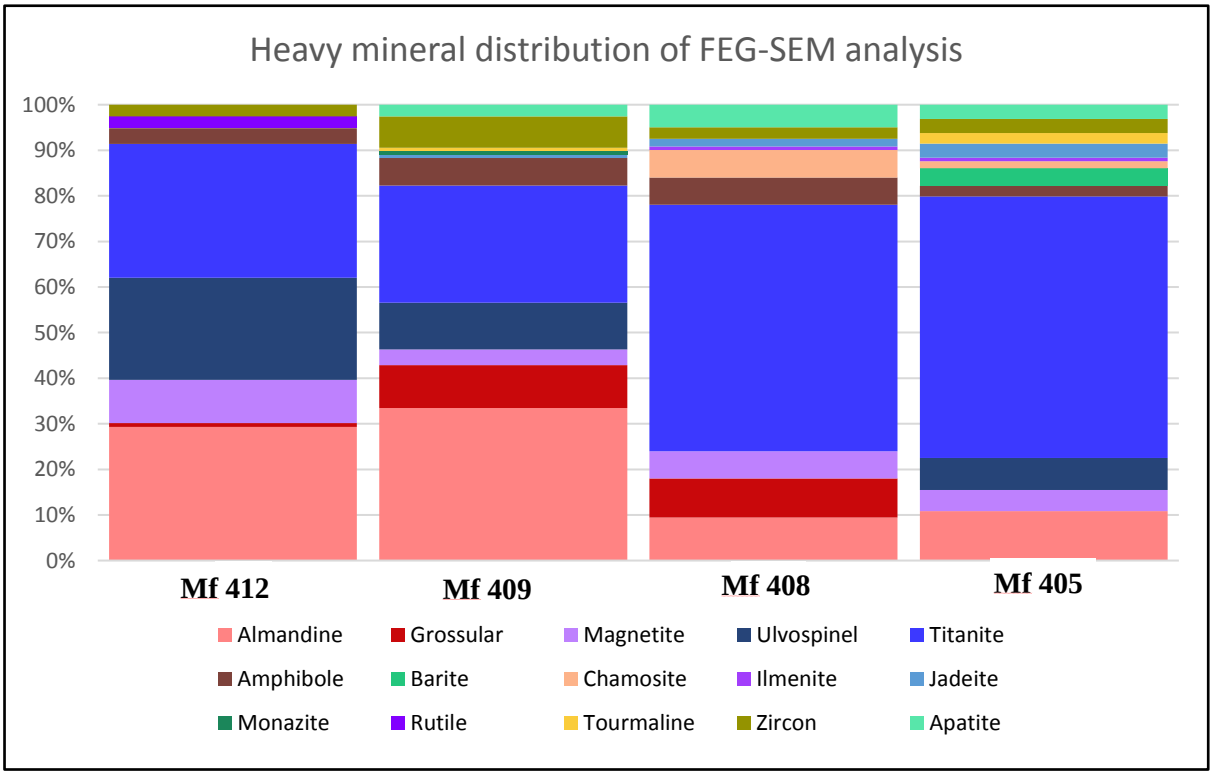

Figure 21: Heavy mineral distribution of magnetic fractions that was carried out by FEG-SEM analysis

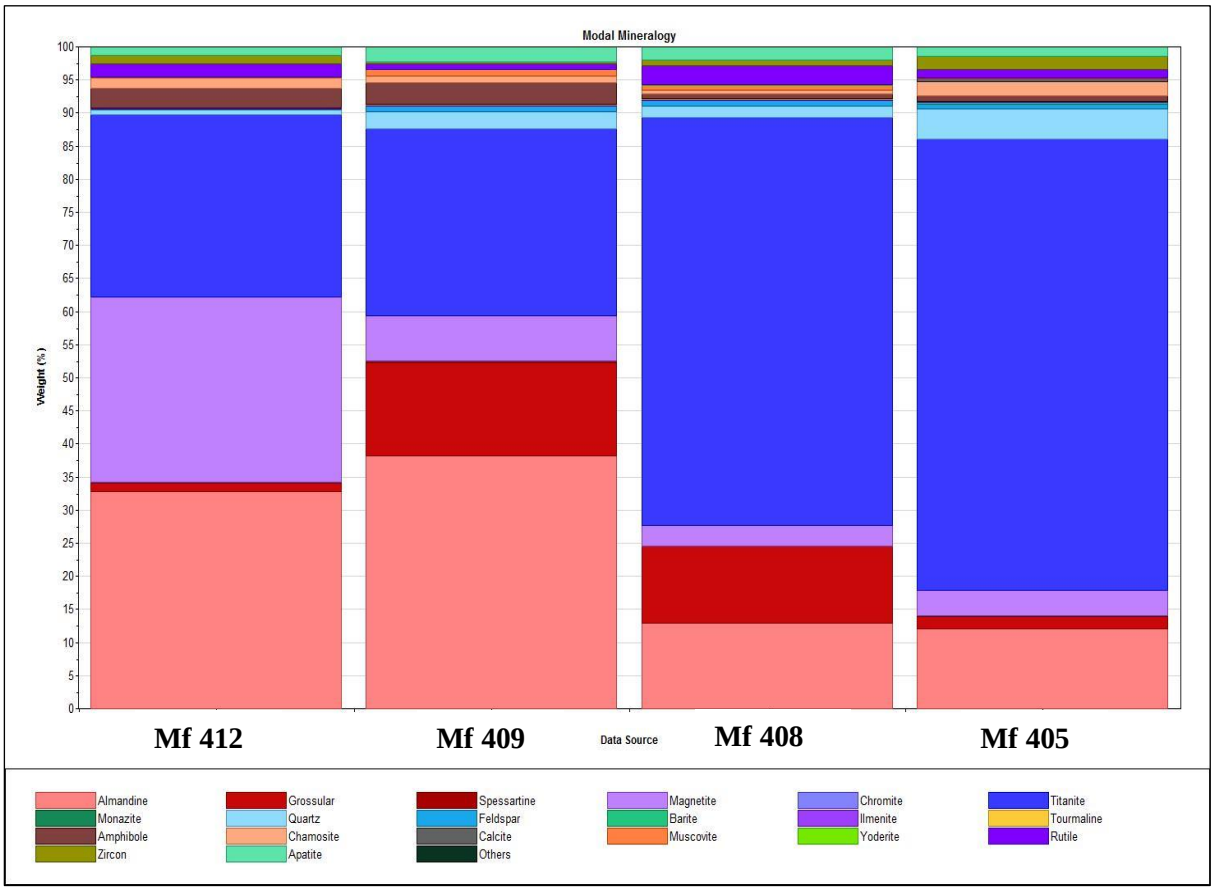

Figure 22: Mineral distribution of the magnetic fractions from MLA analysis.

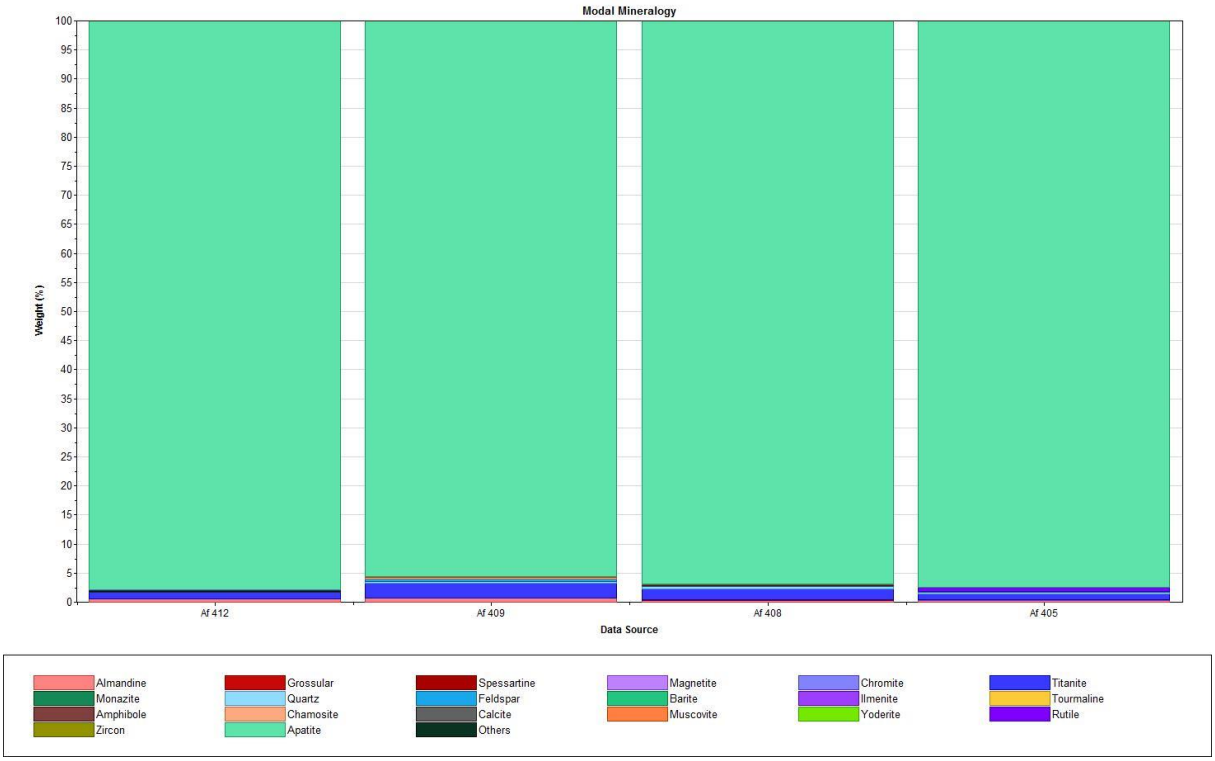

Figure 22: Mineral distribution of the apatite fractions from MLA analysis.

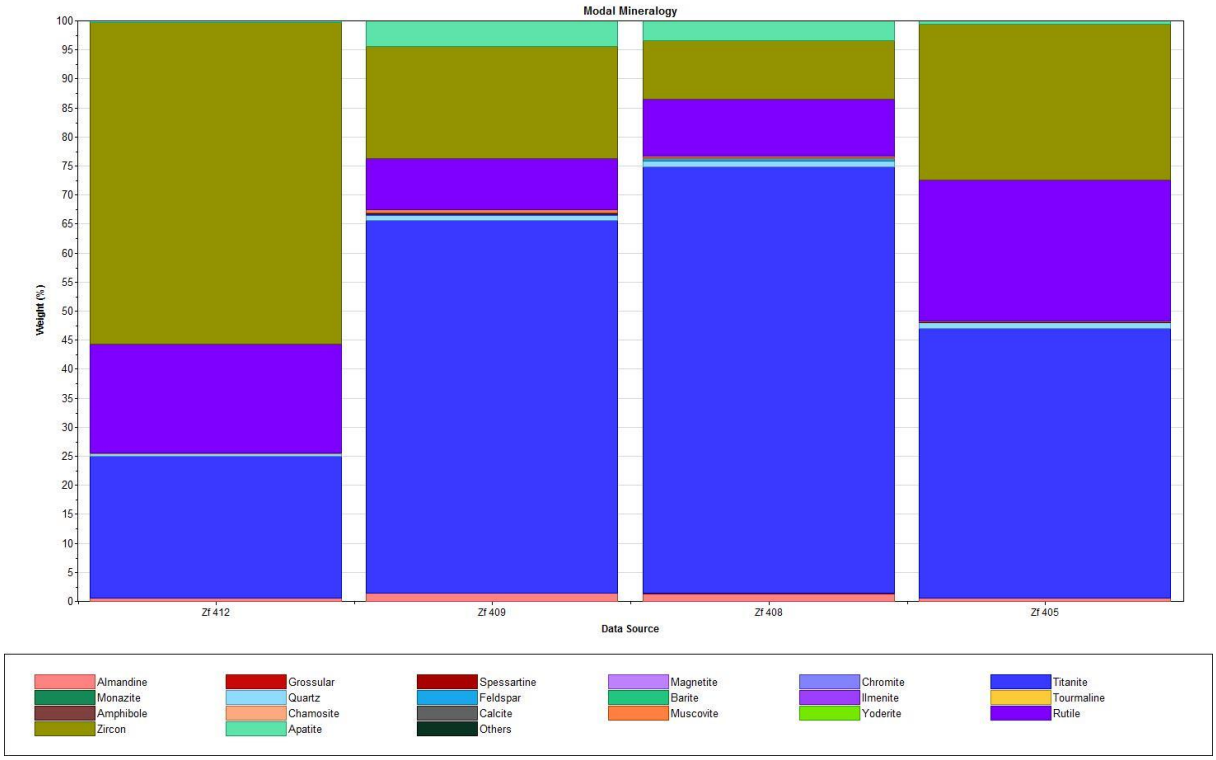

Figure 23: Mineral distribution of the zircon fractions from MLA analysis.

The data from FEG-SEM analysis for garnets have been plotted in the ternary diagrams of figure 25. Worth noting is the Mn+Fe-rich garnets that includes spessartine and almandines, and the Ca-rich comprises grossular and the Mg-rich is indicative of pyrope Morton et al. (2004). The findings of this project can generally be assigned to the Type B and type D groups. Although the garnet types reflect natural sedimentary groupings, observations of modern and ancient sediments indicate that they can be facie related. Garnets of type B are typically associated with amphibolite-facies metasedimentary rocks, whereas Type D represent metasomatic rocks i.e. skarn, very low grade metabasic rocks or calc-silicate granulite from ultra-high temperature metamorphism (Mange and Morton, 2007).

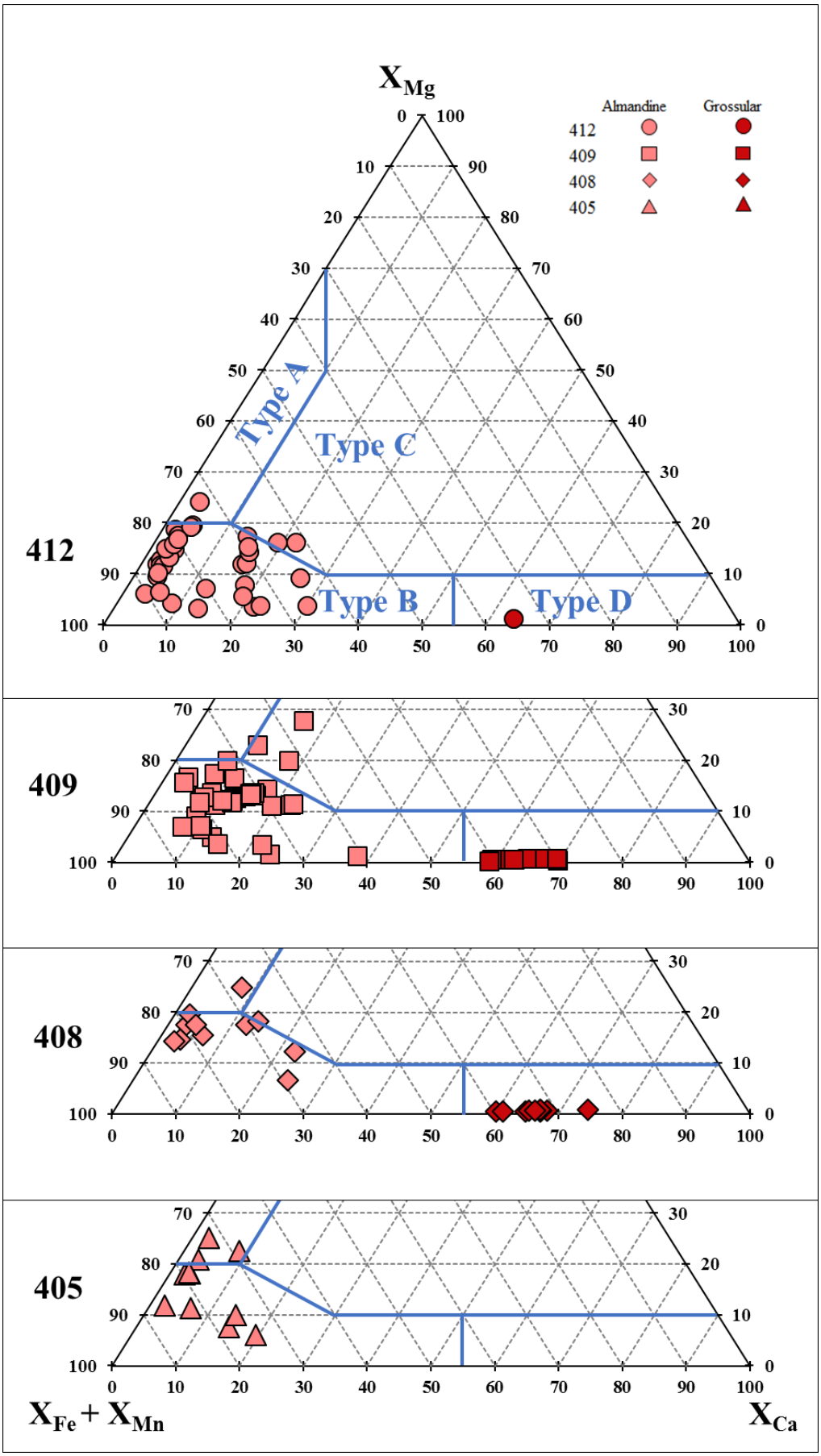

Figure 24: Ternary diagram of garnet composition from sample 412-405 after Mange and Morton (2007).

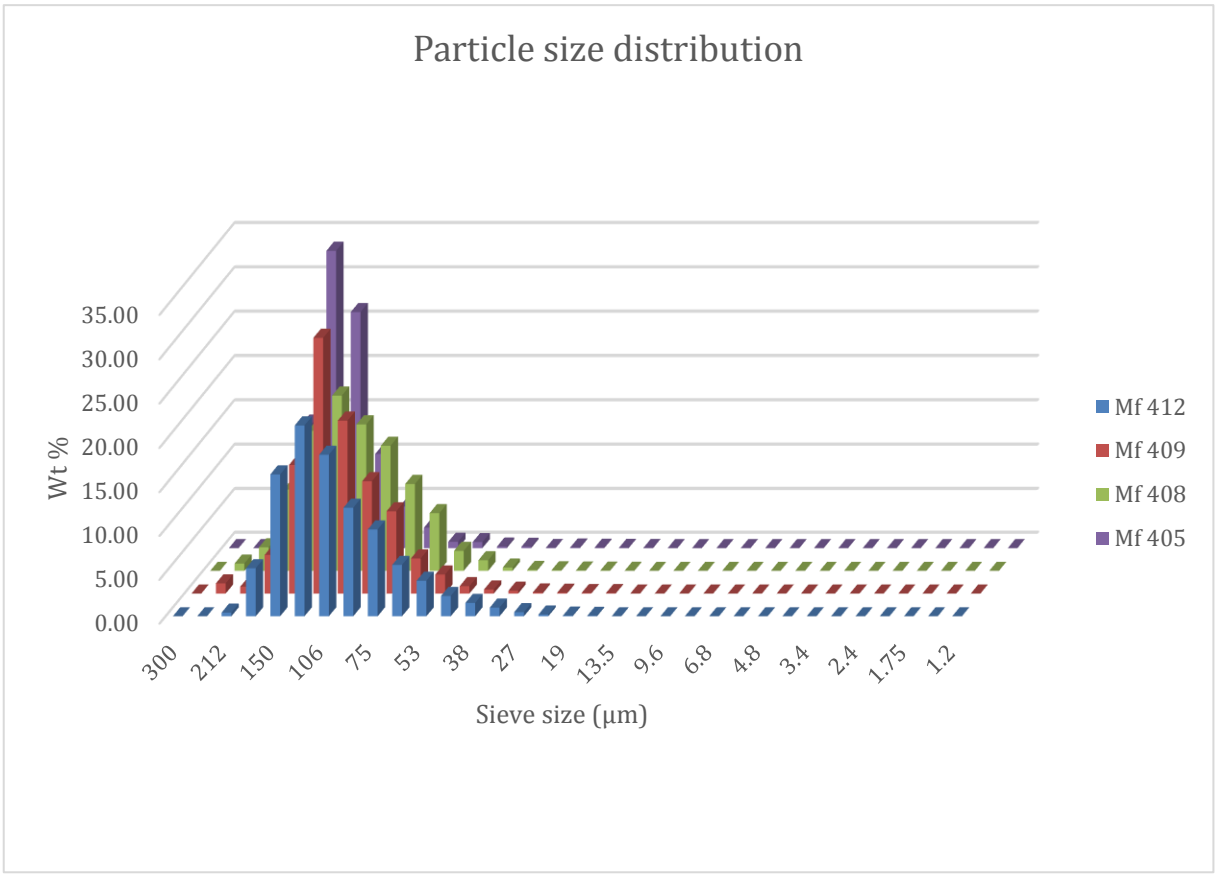

Figure 25: Particle size distribution of the magnetic fractions (Mf).

Sample 412 generally shows the smallest particle size distribution, and sample 405 shows the largest particle size distribution, according to figure 26 for the magnetic fraction. The particle size distribution of the apatite fractions in Figure 27, however, suggests that sample 408 has the smallest particles. Finally, same 409 shows the smallest particle size distribution of the zircon fractions (figure 28), whereas sample 405 has the largest distribution. All fractions show a normal distribution for the respective samples, except for Zf 409. This could indicate a change in the energy level or a small change in provenance of the river where the sediments were deposited.

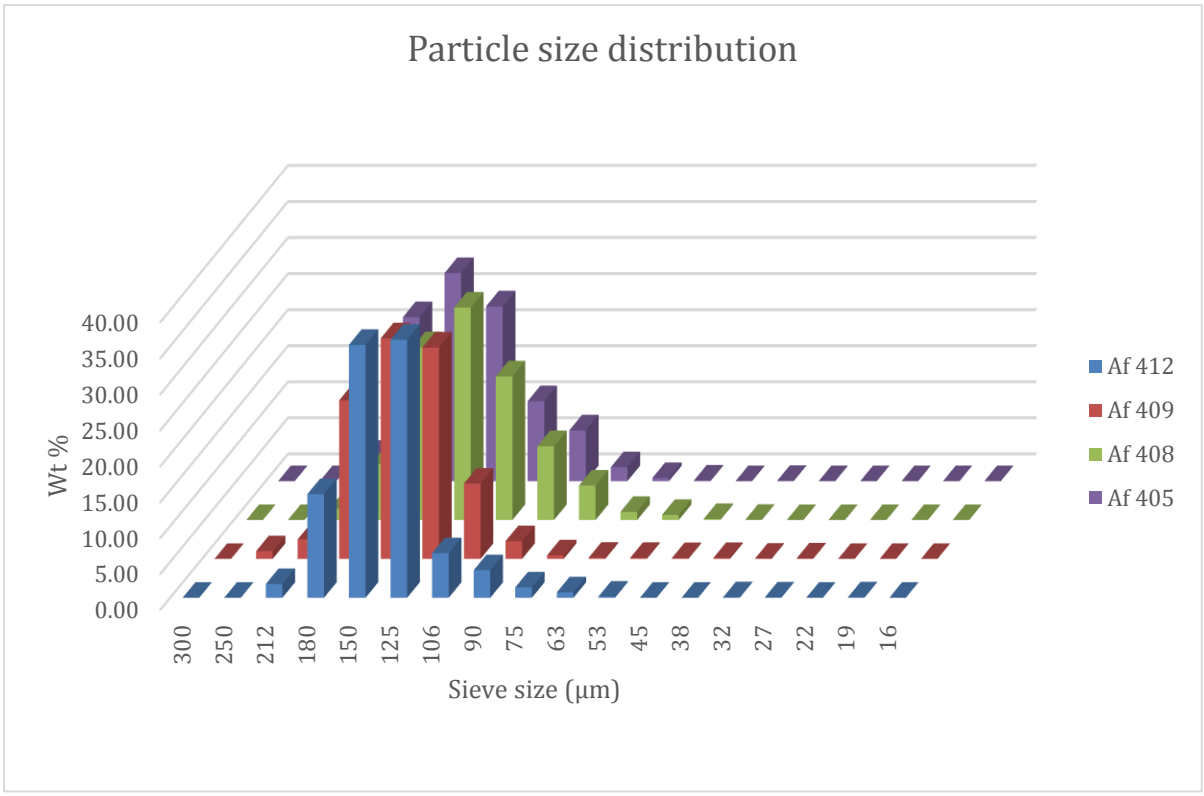

Figure 26: Particle size distribution of the apatite fractions (Af).

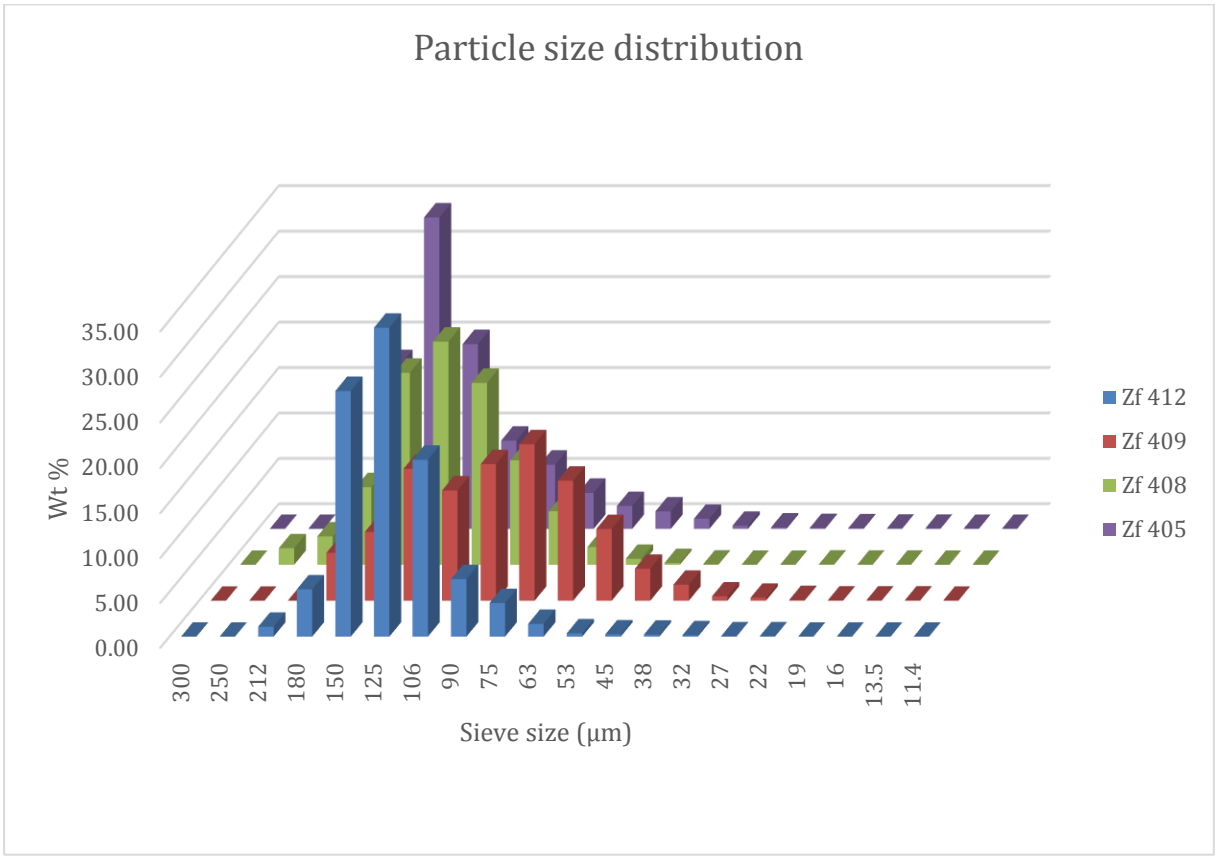

Figure 27: Particle size distribution of the zircon fractions (Zf).

4.2. XRD

The XRD results generally confirms the mineral identification that was carried out by MLA and FEG-SEM analyses. In addition to zircon and quartz, results from XRD analysis suggests presence of the garnet types almandine, grossular and spessartine. Furthermore, apatite is distinguished as fluorapatite for all four samples. Amphibole in form of gedrite can be found in all samples in addition to barroisite that can be found in sample 405 exclusively. Moreover, presence of the minerals hematite, magnetite, spinel and ulvospinel were confirmed. The four samples are all composed of the chamosite (Fe-rich chlorite) besides clinochlore, which is only present in sample 405. Additionally, sample 412 seem to contain diopside.

Conclusion

High resolution heavy mineral studies have been performed on four samples and their associated mineral fractions from Lower Cambrian rocks. The samples have been collected in southeastern Namibia and belong to the Haribes Member of the Nababis Formation, which are part of the Nama Group (Fish River Subgroup).

As the separated heavy minerals are rather large (>250 microns) at most, and as the grains are mostly sub-angular to angular, a rather short transportation can be inferred. Moreover, the particle curves for the samples, with one exception, show one trend. Here, the particle size shows normal distribution with peaks at 125-150 microns. The exception, Zf 409, displays a bimodal trend, with peaks at 75 microns and 125 microns. However, the corresponding apatite and magnetite fraction show similar normalized properties as those above. Previous studies, e.g. Blanco et al. (2011), suggest northern provenance source from the Damara Orogen and a western provenance from the Gariep Belt based on paleocurrents after Germs (1983) and heavy mineral analysis (Blanco et al., 2006;2011). However, the size and angularity of the grains

found in this project suggests that transportation from these sources would be too distant for a braided fluvial depositional environment.

The mineralogy suggests metamorphic origin, i.e. chamosite, garnets, clinopyroxene, as well as the possibility of the identified grossular are Ca-epidotes according to XRD analysis. Generally, XRD, MLA and FEG-SEM analysis illustrate similar mineralogy with some natural variations that could be explained by the river systems in 3D space and time, with large quantities of nesosilicates and oxides/hydroxides (magnetic and zircon fractions), and phosphates (apatite fractions). Due to the constraints of mineral shape, different zircons should be dated to provide a more accurate age and more prominent provenance. Moreover, garnets suggest a primary source of metamorphic amphibole facies origin, although, granitoids and associated pegmatites can also provide garnet-rich sediments (Mange and Morton, 2007). And additionally, supporting the above made suggestion, several of the identified and quantified heavy minerals are rather fragile and would not be able to transport longer distances.

The different methodologies involved in this project, FEG-SEM and MLA, show the same result trends. Yet, the MLA shows an efficient workflow to produce a quantitative analysis of minerals. Additionally, the XRD results show similar findings as the FEG-SEM/MLA, although the XRD suggests gedrite (amphibole group), as well as epidotes, as discussed earlier. Further, diopside (clinopyroxene) was reported in sample 412 exclusively. Moreover, barroisite (amphibole group) was identified by the XRD, only for sample 405, which is the sample with the least garnets.

To conclude, this project has shown that multiple methodologies can be used to reduce uncertainty and provide a greater understanding of heavy mineral distribution and provenance. It is evident, however, that more research needs to be done. Nonetheless, MLA proved to be an

efficient method in determining mineral composition as well as variations in particle size and shape for the respective samples.

Further work

On general basis, a thorough EMPA (Electron Microprobe Analysis) can be recommended to efficiently distinguish between different mineral types that have similar characteristics in SEM/MLA. Moreover, thin sections could be analyzed using optical microscopes to evaluate diageneses as well for estimating grain size, shape and sorting. These are crucial aspects that can be implemented with the conducted MLA analysis to determine the reliability a northern and/or western provenance source. Lastly, whole rock geochemistry should be performed to further determine the degree of sediment recycling and more accurately pin point provenance with more detail combined with age dating of the separated, datable, heavy minerals.

References

Aceñolaza, G. F., Germs, G. J., and Aceñolaza, F. G., 2009, Trace Fossils and the Agronomic Revolution at the Neoproterozoic-Cambrian Transition in Southwest Gondwana: Developments in Precambrian Geology, v. 16, p. 339-347.

Amthor, J. E., Grotzinger, J. P., Schröder, S., Bowring, S. A., Ramezani, J., Martin, M. W., and Matter, A., 2003, Extinction of Cloudina and Namacalathus at the Precambrian-Cambrian boundary in Oman: Geology, v. 31, no. 5, p. 431-434.

Bekkum, J. and Egeland, D., 2016, Testing the validity of EDS analysis at a FE-SEM for quantification of major elements in rock samples related to EOR experiments. Bachelor Thesis, University of Stavanger, Stavanger, 62 pp.

Blanco, G., 2010, Provenance of the Ediacaran-Early Palaeozoic Arroyo del Soldado Group (Uruguay) and The Nama Group (Namibia). Geodynamic implications for the SW-Gondwana amalgamation: Serie Correlación Geológica, v. 26, p. 9-25.

Blanco, G., Abre, P., Rajesh, H., and Germs, G., 2014, Geochemistry and heavy minerals analyses on "black sands" of the lower Cambrian fish river subgroup (Nama group, Namibia): South African Journal of Geology, v. 117, no. 1, p. 129-148.

Blanco, G., Germs, G., Rajesh, H., Chemale, F., Dussin, I., and Justino, D., 2011, Provenance and paleogeography of the Nama Group (Ediacaran to early Palaeozoic, Namibia): petrography, geochemistry and U–Pb detrital zircon geochronology: Precambrian Research, v. 187, no. 1, p. 15-32.

Blanco, G., Rajesh, H., Gaucher, C., Germs, G. J., and Chemale, F., 2009, Provenance of the Arroyo del Soldado Group (Ediacaran to Cambrian, Uruguay): implications for the paleogeographic evolution of southwestern Gondwana: Precambrian Research, v. 171, no. 1, p. 57-73.

Buatois, L. A., Almond, J., and Germs, G. J., 2013, Environmental tolerance and range offset of Treptichnus pedum: Implications for the recognition of the Ediacaran-Cambrian boundary: Geology, v. 41, no. 4, p. 519-522.

Dalziel, I. W., 1991, Pacific margins of Laurentia and East Antarctica-Australia as a conjugate rift pair: Evidence and implications for an Eocambrian supercontinent: Geology, v. 19, no. 6, p. 598-601.

Davies, C., and Coward, M., 1982, The structural evolution of the Gariep arc in southern Namibia (South-West Africa): Precambrian Research, v. 17, no. 3-4, p. 173-198.

Egerton, R. F., 2005, Physical principles of electron microscopy, Springer.

Emery, D., and Robinson, A., 1993, Inorganic Geochemistry: Applications to Petroleum Geology. Blackwells, Oxford.

Fandrich, R., Gu, Y., Burrows, D., and Moeller, K., 2007, Modern SEM-based mineral liberation analysis: International Journal of Mineral Processing, v. 84, no. 1, p. 310-320.

Figueroa, G., Moeller, K., Buhot, M., Gloy, G., and Haberla, D., Advanced discrimination of hematite and magnetite by automated mineralogy, *in* Proceedings Proceedings of the 10th International Congress for Applied Mineralogy (ICAM)2012, Springer, p. 197-204.

Frimmel, H., Basei, M., and Gaucher, C., 2011, Neoproterozoic geodynamic evolution of SW-Gondwana: a southern African perspective: International Journal of Earth Sciences, v. 100, no. 2-3, p. 323-354.

Frimmel, H., and Frank, W., 1998, Neoproterozoic tectono-thermal evolution of the Gariep Belt and its basement, Namibia and South Africa: Precambrian Research, v. 90, no. 1, p. 1-28.

Germs, G J., and Gresse, P., 1991, The foreland basin of the Damara and Gariep orogens in Namaqualand and southern Namibia: stratigraphic correlations and basin dynamics: South African Journal of Geology, v. 94, no. 2-3, p. 159-169.
Germs, G. J., 1972, The stratigraphy and paleontology of the lower Nama Group, South West Africa, University of Cape Town, Dept. of Geology.
Germs, G. J., 1974, The Nama Group in south west Africa and its relationship to the Pan-African geosyncline: The Journal of Geology, v. 82, no. 3, p. 301-317.
Germs, G. J., 1983, Implications of a sedimentary facies and depositional environmental analysis of the Nama Group in South West Africa/Namibia: Geological Society of South Africa, Special Publication, v. 11, p. 89-114.
Germs, G. J., 1995, The Neoproterozoic of southwestern Africa, with emphasis on platform stratigraphy and paleontology: Precambrian Research, v. 73, no. 1-4, p. 137-151.
Germs, G. J., Miller, R. M., Frimmel, H. E., and Gaucher, C., 2009, Syn-to Late-Orogenic Sedimentary Basins of Southwestern Africa$: Neoproterozoic-Cambrian Tectonics, Global Change and Evolution: A Focus on South Western Gondwana/Eds C. Gaucher, AN Sial, HE Frimmel, GP Halverson. Amsterdam: Elsevier Science, p. 183-203.
Geyer, G., 2005, The Fish River Subgroup in Namibia: stratigraphy, depositional environments and the Proterozoic–Cambrian boundary problem revisited: Geological Magazine, v. 142, no. 05, p. 465-498.
Geyer, G., and Uchman, A., 1995, Ichnofossil assemblages from the Nama Group (Neoproterozoic-Lower Cambrian) in Namibia and the Proterozoic-Cambrian boundary problem revisited: Beringeria Special Issue, v. 2, p. 175-202.
Grant, S., 1990, Shell structure and distribution of Cloudina, a potential index fossil for the terminal Proterozoic: American journal of science, v. 290, p. 261.
Gray, D. R., Foster, D. A., Goscombe, B., Passchier, C. W., and Trouw, R. A., 2006, 40 Ar/39 Ar thermochronology of the Pan-African Damara Orogen, Namibia, with implications for tectonothermal and geodynamic evolution: Precambrian research, v. 150, no. 1, p. 49-72.
Gresse, P., and Germs, G., 1993, The Nama foreland basin: sedimentation, major unconformity bounded sequences and multisided active margin advance: Precambrian Research, v. 63, no. 3-4, p. 247259-252272.
Gresse, P. G., 1992, The tectono-sedimentary history of the Vanrhynsdorp Group, Government Printer.
Grotzinger, J., Adams, E., and Schröder, S., 2005, Microbial–metazoan reefs of the terminal Proterozoic Nama Group (c. 550–543 Ma), Namibia: Geological Magazine, v. 142, no. 05, p. 499-517.
Grotzinger, J. P., 2000, Facies and paleoenvironmental setting of thrombolite-stromatolite reefs, terminal Proterozoic Nama Group (ca. 550–543 Ma), central and southern Namibia: Communications of the Geological Survey of Namibia, v. 12, p. 221-233.
Grotzinger, J. P., Bowring, S. A., Saylor, B. Z., and Kaufman, A. J., 1995, Biostratigraphic and geochronologic constraints on early animal evolution: SCIENCE-NEW YORK THEN WASHINGTON-, p. 598-598.
Hardy, R., and Tucker, M., 1988, X-ray powder diffraction of sediments: Techniques in sedimentology, p. 191-228.
Hegenberger, W., 1993, Stratigraphy and sedimentology of the Late Precambrian Witvlei and Nama Groups, east of Windhoek, Geological Survey of Namibia, Ministry of Mines and Energy.
Knoll, A., Vestiges of a beginning? Paleontological and geochemical constraints on early animal evolution, *in* Proceedings Annales de paléontologie2003, Volume 89, Elsevier, p. 205-221.

Mange, M. A., and Morton, A. C., 2007, Geochemistry of heavy minerals: Developments in sedimentology, v. 58, p. 345-391.
McFadden, K. A., Huang, J., Chu, X., Jiang, G., Kaufman, A. J., Zhou, C., Yuan, X., and Xiao, S., 2008, Pulsed oxidation and biological evolution in the Ediacaran Doushantuo Formation: Proceedings of the National Academy of Sciences, v. 105, no. 9, p. 3197-3202.
Meert, J. G., Eide, E. A., and Torsvik, T. H., 1997, The Nama Group revisited: Geophysical journal international, v. 129, no. 3, p. 637-650.
Miller, R. M., 1983, The Pan-African Damara Orogen of South West Africa/Namibia, Evolution of the Damara Orogen of South West Africa/Namibia.
Morton, A., Hallsworth, C., and Chalton, B., 2004, Garnet compositions in Scottish and Norwegian basement terrains: a framework for interpretation of North Sea sandstone provenance: Marine and Petroleum Geology, v. 21, no. 3, p. 393-410.
Saylor, B. Z., Kaufman, A. J., Grotzinger, J. P., and Urban, F., 1998, A composite reference section for terminal Proterozoic strata of southern Namibia: Journal of Sedimentary Research, v. 68, no. 6.
Shaffer, M., Discrimination of hematite and magnetite and quantifying their associations using the JKTECH Mineral Liberation AnalyzerTM, *in* Proceedings The 48th Annual Conference of Metallurgists, Laurentian University, Sudbury, Ontario2009, Volume 73.
Stanistreet, I. G., Kukla, P. A., and Henry, G., 1991, Sedimentary basinal responses to a late precambrian Wilson Cycle: the Damara Orogen and Nama foreland, Namibia: Journal of African Earth Sciences (and the Middle East), v. 13, no. 1, p. 141-156.
Sylvester, P. J., 2012, Use of the mineral liberation analyzer (MLA) for mineralogical studies of sediments and sedimentary rocks: Quantitative Mineralogy and Microanalysis of Sediments and Sedimentary Rocks (P. Sylvester, ed.). Mineralogical Association of Canada Short Course Series, v. 42, p. 1-16.
Wood, R., Poulton, S., Prave, A., Hoffmann, K.-H., Clarkson, M., Guilbaud, R., Lyne, J., Tostevin, R., Bowyer, F., and Penny, A., 2015, Dynamic redox conditions control late Ediacaran metazoan ecosystems in the Nama Group, Namibia: Precambrian Research, v. 261, p. 252-271.
Wood, R. A., Grotzinger, J. P., and Dickson, J., 2002, Proterozoic modular biomineralized metazoan from the Nama Group, Namibia: Science, v. 296, no. 5577, p. 2383-2386.

Appendix A – Heavy mineral garnet data using FEG-SEM.

Identification of garnets in samples using EDS												
Sample name	Fraction	Garnet type	Color code	Wt%								
				O	Mg	Al	Si	Ca	Ti	Mn	Fe	Total
412	Magnetic	Almandine		39.99	3.54	12.22	18.13	0.71	0.08	0.11	25.22	100
412	Magnetic	Almandine		43.01	3.27	12.04	17.7	4.28	0.09	0.35	19.26	100
412	Magnetic	Almandine		43.35	2.12	12.14	17.59	4.91	0.04	0.43	19.42	100
412	Magnetic	Grossular		38.75	0.31	14.36	21.62	16.06	0.07	0.09	8.74	100
412	Magnetic	Almandine		45.45	4.91	11.85	17.51	1.06	0.12	0.12	18.98	100
412	Magnetic	Almandine		44.51	1.91	11.82	17.44	3.25	0.01	1.84	19.22	100
412	Magnetic	Almandine		46.25	2.99	11.68	17.53	4	0.00	0.30	17.25	100
412	Magnetic	Almandine		42.62	3.95	11.92	18.11	4.28	0.02	0.35	18.75	100
412	Magnetic	Almandine		39.02	3.87	12.39	18.62	0.75	0.02	0.24	25.09	100
412	Magnetic	Almandine		39.28	5.47	12.55	18.95	0.57	0.01	0.07	23.1	100
412	Magnetic	Almandine		40.26	4.32	12.27	18.38	1.07	0.02	0.24	23.44	100
412	Magnetic	Almandine		37.96	1.4	12.14	18.26	2.72	0.01	1.43	26.08	100
412	Magnetic	Almandine		38.36	1.18	12.45	18.85	9.09	0.01	0.84	19.22	100
412	Magnetic	Almandine		36.75	3.71	12.71	19.04	0.97	0.01	0.23	26.58	100
412	Magnetic	Almandine		38.19	4.74	12.97	19.62	6.46	0.01	0.30	17.71	100
412	Magnetic	Almandine		37.07	5.27	12.89	19.89	4.18	0.02	0.72	19.96	100
412	Magnetic	Almandine		36.19	2.03	12.39	18.61	1.13	0.02	0.74	28.89	100
412	Magnetic	Almandine		34.61	1.17	13.01	19.95	7.05	0.02	1.35	22.84	100
412	Magnetic	Almandine		37.38	2.97	12.6	18.89	1.13	0.01	0.76	26.26	100

412	Magnetic	Almandine		34.8	3.76	13.16	19.94	1.15	0.01	0.42	26.76	100
412	Magnetic	Almandine		38.39	2.81	12.22	19.12	7.93	0.03	1.92	17.58	100
412	Magnetic	Almandine		38.52	3.15	12.42	18.34	1.05	0.01	1.04	25.47	100
412	Magnetic	Almandine		38.53	4.56	12.69	19.12	4.47	0.03	0.48	20.12	100
412	Magnetic	Almandine		37.44	4.03	12.85	19.33	1.13	0.02	0.34	24.86	100
412	Magnetic	Almandine		39.98	1.11	12.29	18.51	6.63	0.04	1.40	20.04	100
412	Magnetic	Almandine		40.89	4.32	12.33	18.12	0.64	0.01	0.19	23.5	100
412	Magnetic	Almandine		40.56	5	12.51	18.55	0.82	0.02	0.28	22.26	100
412	Magnetic	Almandine		40.1	4.6	12.38	18.48	0.9	0.03	0.25	23.26	100
412	Magnetic	Almandine		40.6	0.97	11.64	18.01	3.91	0.01	4.75	20.11	100
412	Magnetic	Almandine		40.55	5.5	12.31	18.64	1.18	0.00	0.20	21.62	100
412	Magnetic	Almandine		38.95	2.01	12.2	18.16	1.69	0.02	0.83	26.14	100
412	Magnetic	Almandine		39.42	4.93	12.63	18.75	0.97	0.02	0.23	23.05	100
412	Magnetic	Almandine		36.04	4.85	13.51	20.67	5.7	0.03	0.35	18.85	100
412	Magnetic	Almandine		29.82	1.9	14.59	22.73	6.25	0.02	1.28	23.41	100
412	Magnetic	Almandine		37.43	7.01	13.36	20.34	0.84	0.01	0.32	20.69	100
409	Magnetic	Almandine		39.26	1.56	11.97	18.24	3.96	0.03	1.26	23.72	100
409	Magnetic	Grossular		44.1	0.12	12.78	18.29	15.2	0.01	0.01	9.49	100.002
409	Magnetic	Almandine		41.21	3.21	12.27	18.65	6.3	0.02	0.40	17.94	100
409	Magnetic	Almandine		40.72	3.62	12.32	18.51	3.69	0.02	0.40	20.72	100
409	Magnetic	Almandine		41.18	3.85	12.26	18.5	4.24	0.01	0.59	19.37	100
409	Magnetic	Grossular		43.23	0.15	13.77	18.55	15.34	0.01	0.15	8.8	100
409	Magnetic	Grossular		43.27	0.15	12.51	18.46	15.27	0.02	0.23	10.09	100
409	Magnetic	Almandine		41.05	4.05	12.29	18.57	4.79	0.03	0.56	18.66	100

409	Magnetic	Almandine		40.65	3.67	12.39	18.8	4.03	0.02	0.42	20.02	100
409	Magnetic	Grossular		44.07	0.16	14.09	18.63	15.2	0.01	0.30	7.54	100
409	Magnetic	Grossular		43.85	0.17	14.61	18.71	15.41	0.02	0.20	7.03	100
409	Magnetic	Grossular		43.77	0.11	13.48	18.49	15.2	0.01	0.21	8.73	100
409	Magnetic	Almandine		42.48	7.12	12.78	19.06	4.14	0.01	0.24	14.17	100
409	Magnetic	Grossular		44.13	0.17	12.84	18.74	15.57	0.22	0.11	8.22	100
409	Magnetic	Almandine		40.49	2.61	12.27	18.38	2.48	0.01	0.73	23.03	100
409	Magnetic	Almandine		40.87	0.46	11.93	18.12	6.96	0.02	1.63	20.01	100
409	Magnetic	Almandine		38.05	4.97	12.8	19.39	1.05	0.02	0.43	23.29	100
409	Magnetic	Almandine		41.58	3.7	12.11	18.25	4.47	0.03	0.36	19.5	100
409	Magnetic	Almandine		40.05	1.04	11.82	18.1	6.55	0.01	0.58	21.85	100
409	Magnetic	Grossular		44.06	0.09	14.88	18.53	15.69	0.03	0.10	6.62	100
409	Magnetic	Almandine		38.26	6.44	13.1	17.9	4.3	0.02	0.42	19.56	100
409	Magnetic	Almandine		36.63	6.58	13.87	20.88	3.25	0.00	0.59	18.2	100
409	Magnetic	Almandine		40.13	4.56	12.35	18.51	0.98	0.02	0.22	23.23	100
409	Magnetic	Grossular		43.72	0.17	15.11	18.91	15.43	0.01	0.16	6.49	100
409	Magnetic	Grossular		42.8	0.36	9.44	18.46	10.72	0.96	2.28	14.98	100
409	Magnetic	Grossular		42.7	0.06	12.58	18.47	15.51	0.01	0.21	10.46	100
409	Magnetic	Almandine		40.67	1.91	12.07	18.18	3.13	0.02	0.38	23.64	100
409	Magnetic	Almandine		40.96	4.86	12.46	18.65	2.03	0.02	0.22	20.8	100
409	Magnetic	Almandine		41.3	4.57	12.19	19.02	2.96	0.02	0.18	19.76	100
409	Magnetic	Almandine		40.8	5.52	12.33	19.34	2.22	0.01	0.42	19.36	100
409	Magnetic	Almandine		35.3	1.14	13	20.23	4.64	0.02	2.25	23.42	100
409	Magnetic	Almandine		38.3	2.16	12.45	19.48	3.05	0.01	0.59	23.96	100
409	Magnetic	Almandine		40.2	3.2	12.87	18.5	5.5	0.02	0.39	19.32	100

409	Magnetic	Almandine		40.72	3.62	12.38	18.41	3.65	0.03	0.50	20.69	100
409	Magnetic	Almandine		41.2	3.85	12.26	18.5	2.45	0.01	0.59	21.14	100
409	Magnetic	Almandine		41.23	3.21	12.5	17.9	6.3	0.02	0.39	18.45	100
409	Magnetic	Almandine		40.72	3.62	12.32	17.4	3.69	0.02	0.40	21.83	100
409	Magnetic	Almandine		41.18	3.85	12.26	18.5	4.24	0.01	0.45	19.51	100
409	Magnetic	Almandine		41.21	3.21	12.27	18.65	6.3	0.02	0.40	17.94	100
409	Magnetic	Almandine		40.72	3.51	11.89	18.51	3.69	0.02	0.40	21.26	100
409	Magnetic	Almandine		42.4	1.92	12.01	18.5	2.03	0.01	0.59	22.54	100
409	Magnetic	Almandine		41.21	3.21	12.27	18.65	2.96	0.02	0.45	21.23	100
409	Magnetic	Almandine		40.72	3.62	12.8	18.51	2.22	0.02	0.41	21.7	100
409	Magnetic	Almandine		41.18	3.85	13	17.9	4.34	0.01	0.59	19.13	100
409	Magnetic	Almandine		41.21	3.21	12.27	18.65	6.3	0.02	0.40	17.94	100
409	Magnetic	Almandine		40.72	3.4	11.94	18.51	3.69	0.03	0.40	21.31	100
409	Magnetic	Almandine		41.18	3.85	12.1	18.5	4.24	0.01	0.59	19.53	100
409	Magnetic	Almandine		43.1	3.21	12.22	18.65	2.96	0.02	0.40	19.44	100
409	Magnetic	Almandine		40.72	3.41	11.97	18.51	2.22	0.02	0.40	22.75	100
409	Magnetic	Almandine		41.18	3.78	12.02	18.5	4.24	0.01	0.59	19.68	100
408	Magnetic	Grossular		24.37	0.21	16.72	23.26	24.14	0.12	0.28	10.9	100
408	Magnetic	Grossular		29.2	0.14	15.43	24.23	20.05	0.11	0.37	10.47	100
408	Magnetic	Almandine		27.04	6.23	13.87	23.51	4.37	0.10	0.97	23.91	100
408	Magnetic	Almandine		28.13	6.1	13.8	23.13	1.01	0.10	0.17	27.56	100
408	Magnetic	Almandine		28.57	6.12	13.79	24.06	4.63	0.08	0.59	22.16	100
408	Magnetic	Almandine		28.28	5.39	13.67	23.29	2.24	0.12	0.46	26.55	100
408	Magnetic	Grossular		30.36	0.17	15.82	23.19	19.82	0.19	0.20	10.25	100
408	Magnetic	Almandine		26.24	5.61	13.12	22.38	1.3	0.12	0.34	30.89	100

408	Magnetic	Grossular		31.73	0.21	18.01	23.61	19.73	0.07	0.39	6.25	100
408	Magnetic	Almandine		30.81	7.28	11.98	28.24	2.32	0.09	0.76	18.52	100
408	Magnetic	Grossular		32.48	0.22	16.12	23.05	18.88	0.09	0.15	9.01	100
408	Magnetic	Almandine		28.35	4.23	13.71	23.4	7.76	0.07	0.39	22.09	100
408	Magnetic	Almandine		29.84	6.62	13.57	22.81	0.78	0.16	0.71	25.51	100
408	Magnetic	Almandine		30.59	2.26	13.12	22.07	8.23	0.32	1.37	22.04	100
408	Magnetic	Grossular		33.91	0.22	15.81	22.38	18.56	0.12	0.36	8.64	100
408	Magnetic	Grossular		36.88	0.13	11.58	27.08	14.63	0.11	0.16	9.43	100
408	Magnetic	Almandine		28.44	5.11	13.31	22.37	0.95	0.13	0.29	29.4	100
408	Magnetic	Grossular		34.15	0.14	14.22	21.97	18.06	0.11	0.20	11.15	100
408	Magnetic	Almandine		29.23	5.95	13.8	23.04	1.47	0.05	0.51	25.95	100
408	Magnetic	Grossular		33.4	0.14	16.09	22.84	18.44	0.10	0.31	8.68	100
408	Magnetic	Grossular		33.95	0.18	15.74	22.74	18.14	0.09	0.21	8.95	100
405	Magnetic	Almandine		38.11	3.72	12.34	18.38	0.72	0.01	0.23	26.49	100
405	Magnetic	Almandine		38.87	2.37	11.94	18.35	4.47	0.02	0.60	23.38	100
405	Magnetic	Almandine		40.81	5.21	12.29	18.36	0.87	0.02	0.13	22.31	100
405	Magnetic	Almandine		40.14	2.93	12.2	18.17	4.24	0.01	0.33	21.98	100
405	Magnetic	Almandine		39.09	3.44	12.27	18.29	2.01	0.01	0.68	24.21	100
405	Magnetic	Almandine		39.21	6.03	12.5	19.5	0.87	0.02	0.18	21.69	100
405	Magnetic	Almandine		37.44	7.42	13.32	19.81	0.78	0.01	0.39	20.83	100
405	Magnetic	Almandine		39.25	1.88	11.98	18.28	5.94	0.01	0.85	21.81	100
405	Magnetic	Almandine		40.72	5.16	12.19	18.3	0.71	0.04	0.14	22.74	100
405	Magnetic	Almandine		41.46	6.19	12.34	18.82	2.34	0.05	0.26	18.54	100
405	Magnetic	Almandine		41.52	5.13	12.08	18.32	0.83	0.04	0.19	21.89	100

Appendix B – Particle size distribution from MLA.

Size Definition: Equivalent Circle
Sieve Size Series: 4 Sqrt 2
Table Type: Size Distribute
Filter:
Unfiltered

Sieve Size	Mf 412 - Retained Wt%	Mf 409 - Retained Wt%	Mf 408 - Retained Wt%	Mf 405 - Retained Wt%
300	0.00	0.00	0.00	0.00
250	0.00	1.16	0.83	0.00
212	0.42	0.79	2.69	5.88
180	5.48	4.42	9.28	14.12
150	16.17	14.65	15.90	33.61
125	21.69	28.98	19.87	26.70
106	18.38	19.64	16.62	10.70
90	12.39	12.81	14.21	4.74
75	9.91	9.38	9.90	2.33
63	5.86	4.01	6.58	0.72
53	4.06	2.18	2.28	0.69
45	2.32	0.85	1.21	0.18
38	1.52	0.47	0.38	0.16
32	0.99	0.33	0.10	0.02
27	0.47	0.13	0.07	0.06
22	0.20	0.10	0.04	0.04
19	0.08	0.06	0.02	0.02
16	0.05	0.06	0.01	0.02
13.5	0.00	0.00	0.00	0.00
11.4	0.00	0.00	0.00	0.00
9.6	0.00	0.00	0.00	0.00
8.1	0.00	0.00	0.00	0.00
6.8	0.00	0.00	0.00	0.00
5.7	0.00	0.00	0.00	0.00
4.8	0.00	0.00	0.00	0.00
4.1	0.00	0.00	0.00	0.00
3.4	0.00	0.00	0.00	0.00
2.9	0.00	0.00	0.00	0.00
2.4	0.00	0.00	0.00	0.00
2	0.00	0.00	0.00	0.00
1.75	0.00	0.00	0.00	0.00
1.45	0.00	0.00	0.00	0.00
1.2	0.00	0.00	0.00	0.00

Data Source: Apatite fraction
Size Definition: Equivalent Circle
Sieve Size Series: 4 Sqrt 2
Table Type: Size Distribute

Sieve Size	Af 412 - Retained Wt%	Af 409 - Retained Wt%	Af 408 - Retained Wt%	Af 405 - Retained Wt%
300	0.00	0.00	0.00	0.00
250	0.00	1.07	0.00	0.00
212	1.91	2.71	1.57	3.52
180	14.46	22.07	7.82	22.74
150	35.18	30.67	24.01	28.86
125	35.89	29.38	29.51	24.25
106	6.21	10.50	19.96	11.09
90	3.84	2.47	10.28	7.04
75	1.45	0.50	4.81	1.94
63	0.75	0.16	1.14	0.43
53	0.15	0.15	0.71	0.09
45	0.00	0.10	0.15	0.00
38	0.00	0.13	0.03	0.04
32	0.07	0.03	0.00	0.00
27	0.03	0.06	0.00	0.00
22	0.00	0.00	0.00	0.00
19	0.06	0.00	0.00	0.00
16	0.00	0.00	0.00	0.00

Data Source: Zircon fraction
Size Definition: Equivalent Circle
Sieve Size Series: 4 Sqrt 2
Table Type: Size Distribute

Sieve Size	Zf 412 - Retained Wt%	Zf 409 - Retained Wt%	Zf 408 - Retained Wt%	Zf 405 - Retained Wt%
300	0.00	0.00	0.00	0.00
250	0.00	0.00	1.84	0.00
212	1.10	0.00	3.16	0.00
180	5.26	5.32	8.62	18.16
150	27.21	7.67	21.21	34.30
125	34.16	14.64	24.64	20.37
106	19.64	12.26	20.10	9.74
90	6.40	15.15	11.57	7.10
75	3.74	17.35	5.96	4.00
63	1.43	13.34	1.97	2.54
53	0.37	7.98	0.67	1.94
45	0.25	3.55	0.19	1.13
38	0.22	1.78	0.03	0.35
32	0.15	0.48	0.00	0.16
27	0.04	0.33	0.00	0.09
22	0.03	0.08	0.02	0.07
19	0.00	0.03	0.01	0.02
16	0.00	0.02	0.01	0.02
13.5	0.00	0.02	0.00	0.00
11.4	0.00	0.00	0.00	0.00

Appendix C – Mineral distribution from MLA analysis.

Data Source: Magnetic fraction
Mineral Groupings: Ungrouped
Filter: Unfiltered

Mineral	Mf 412 - Wt%	Mf 409 - Wt%	Mf 408 - Wt%	Mf 405 - Wt%	Mf 412 - Particle Count	Mf 409 - Particle Count	Mf 408 - Particle Count	Mf 405 - Particle Count	Mf 412 - Grain Count	Mf 409 - Grain Count	Mf 408 - Grain Count	Mf 405 - Grain Count
Quartz	0.90	3.78	1.97	5.15	127	299	240	206	200	543	406	379
Albite	0.10	0.63	0.44	0.48	36	134	107	67	45	204	187	119
Orthoclase	0.09	0.51	0.53	0.32	16	174	142	41	18	273	248	78
Calcite	0.04	0.00	0.02	0.40	6	2	4	18	8	3	4	35
Chamosite	1.53	1.06	0.45	2.16	411	417	288	270	804	981	541	583
Muscovite	0.06	0.97	0.86	0.22	21	343	334	29	24	606	550	60
Amphibole	2.99	3.27	0.74	0.83	139	229	98	70	249	432	153	119
Yoderite	0.00	0.00	0.09	0.00	0	1	2	0	0	2	2	0
Tourmaline	0.00	0.10	0.21	0.02	3	70	55	11	4	82	59	18
Almandine-Mn	3.34	2.48	0.97	0.84	158	247	113	77	340	472	177	158
Almandine-Ca1	16.97	19.53	6.85	6.44	680	712	546	360	1208	1377	947	1037
Almandine-Ca4	5.24	5.56	1.51	1.93	303	359	157	228	734	943	262	455
Almandine-Ca5	6.73	9.43	3.09	2.58	531	610	471	347	1024	1332	778	805
Almandine-Ca9	0.48	0.55	0.48	0.20	103	198	225	94	135	289	280	121
Grossular-Fe	0.82	7.63	5.11	1.27	29	214	185	33	65	587	490	113
Grossular	0.39	6.09	6.34	0.67	23	212	182	32	84	714	531	141
Spessartine-Ca	0.04	0.09	0.01	0.10	5	7	4	2	6	13	4	9
Spessartine	0.07	0.24	0.00	0.00	2	1	0	0	2	1	0	0
Spessartine-Fe	0.08	0.00	0.00	0.00	3	1	0	2	10	1	0	2
Magnetite	15.92	4.16	1.66	2.75	404	186	76	66	745	338	118	131
Magnetite-Ti	11.98	2.58	1.46	1.06	310	148	72	70	718	286	138	168
Ilmenite	0.17	0.20	0.09	0.07	58	14	25	28	133	32	43	71
Rutile	2.10	0.84	2.82	1.25	123	29	68	86	237	54	191	185
Chromite	0.01	0.00	0.00	0.00	1	0	0	0	1	0	0	0
Chromite-Mn	0.00	0.00	0.00	0.00	0	0	0	0	0	0	0	0
Titanite	23.75	26.50	60.44	64.20	726	614	874	548	1269	1035	1214	885
Titanite-Fe	3.71	1.24	1.00	3.46	399	229	220	334	1242	466	375	1200
Zircon	1.26	0.26	0.88	1.84	47	36	47	21	50	43	52	22
Apatite	1.23	2.26	1.96	1.46	49	64	59	38	62	74	66	56
Barite	0.00	0.00	0.00	0.29	0	0	0	17	0	0	0	37
Monazite-Ce	0.00	0.00	0.00	0.00	0	0	0	1	0	0	0	1
NdLaCaThSmSiFeO	0.00	0.03	0.02	0.00	2	10	9	1	3	33	41	1
SiC	0.00	0.00	0.00	0.02	8	13	11	22	9	14	12	25
Unknown	0.00	0.00	0.00	0.00	1	6	4	7	1	6	4	7
Low_Counts	0.00	0.00	0.00	0.00	0	0	0	0	0	0	0	0
No_XRay	0.00	0.00	0.00	0.00	1	0	0	0	1	0	0	0
Total	100.00	100.00	100.00	100.00	1442	1302	1210	650	9431	11236	7873	7021

Data Source: Apatite fraction
Mineral Groupings: Ungrouped
Filter: Unfiltered

Mineral	Af 412 - Wt%	Af 409 - Wt%	Af 408 - Wt%	Af 405 - Wt%	Af 412 - Particle Count	Af 409 - Particle Count	Af 408 - Particle Count	Af 405 - Particle Count	Af 412 - Grain Count	Af 409 - Grain Count	Af 408 - Grain Count	Af 405 - Grain Count
Quartz	2.52	0.72	0.54	0.35	6	20	25	9	23	32	39	15
Albite	0.00	0.33	0.23	0.39	1	17	10	8	1	31	10	20
Orthoclase	0.00	0.22	0.21	0.04	0	12	10	4	0	32	26	9
Calcite	0.00	0.01	0.01	0.01	0	5	2	1	0	5	3	2
Chamosite	0.07	0.26	0.02	0.09	6	14	12	12	8	19	17	15
Muscovite	0.03	0.15	0.17	0.00	3	36	33	1	5	47	45	1
Amphibole	0.02	0.01	0.01	0.03	3	3	2	4	3	3	2	4
Yoderite	0.00	0.00	0.00	0.00	0	0	0	0	0	0	0	0
Tourmaline	0.00	0.01	0.01	0.00	0	3	3	0	0	3	3	0
Almandine-Mn	0.02	0.01	0.01	0.01	1	4	2	1	1	4	2	1
Almandine-Ca1	0.25	0.42	0.19	0.19	18	35	23	22	24	44	25	29
Almandine-Ca4	0.02	0.02	0.01	0.01	3	4	4	2	3	5	4	2
Almandine-Ca5	0.21	0.14	0.09	0.11	17	34	18	19	24	36	19	20
Almandine-Ca9	0.02	0.06	0.05	0.01	3	17	13	3	3	17	14	3
Grossular-Fe	0.01	0.01	0.03	0.01	1	3	6	1	2	3	7	2
Grossular	0.00	0.01	0.03	0.00	0	2	6	1	0	3	8	1
Spessartine-Ca	0.00	0.00	0.00	0.00	0	0	0	1	0	0	0	1
Spessartine	0.00	0.00	0.00	0.00	0	0	0	0	0	0	0	0
Spessartine-Fe	0.00	0.00	0.00	0.00	0	0	0	0	0	0	0	0
Magnetite	0.00	0.02	0.00	0.04	0	6	4	2	0	7	5	5
Magnetite-Ti	0.00	0.00	0.00	0.00	0	0	1	1	0	0	1	1
Ilmenite	0.00	0.00	0.00	0.00	0	1	0	0	0	1	0	0
Rutile	0.11	0.00	0.00	0.66	3	1	0	1	6	1	0	2
Chromite	0.00	0.00	0.00	0.00	0	0	0	0	0	0	0	0
Chromite-Mn	0.00	0.00	0.00	0.00	0	0	0	0	0	0	0	0
Titanite	1.19	2.58	1.87	1.13	4	24	27	14	5	35	37	26
Titanite-Fe	0.01	0.00	0.01	0.00	1	1	1	0	1	1	1	0
Zircon	0.02	0.03	0.03	0.03	2	11	11	6	6	17	14	10
Apatite	95.49	95.00	96.46	96.86	116	259	379	219	116	260	383	219
Barite	0.00	0.00	0.00	0.03	0	0	0	1	0	0	0	8
Monazite-Ce	0.01	0.00	0.00	0.00	2	0	0	0	2	0	0	0
NdLaCaThSmSiFeO	0.00	0.00	0.00	0.00	0	0	0	0	0	0	0	0
SiC	0.00	0.00	0.00	0.00	1	2	4	1	2	2	4	1
Unknown	0.00	0.00	0.00	0.00	0	0	0	0	0	0	0	0
Low_Counts	0.00	0.00	0.00	0.00	0	0	0	0	0	0	0	0
No_XRay	0.00	0.00	0.00	0.00	0	0	0	1	0	0	0	1
Total	100.00	100.00	100.00	100.00	124	285	400	226	235	608	669	398

Data Source: Zircon fraction
Mineral Groupings: Ungrouped
Filter: Unfiltered

Mineral	Zf 412 - Wt%	Zf 409 - Wt%	Zf 408 - Wt%	Zf 405 - Wt%	Zf 412 - Particle Count	Zf 409 - Particle Count	Zf 408 - Particle Count	Zf 405 - Particle Count	Zf 412 - Grain Count	Zf 409 - Grain Count	Zf 408 - Grain Count	Zf 405 - Grain Count
Quartz	0.45	1.20	0.96	1.02	24	67	51	57	34	82	78	73
Albite	0.01	0.25	0.19	0.02	3	29	27	5	3	33	38	7
Orthoclase	0.00	0.24	0.30	0.01	1	43	34	2	2	55	57	2
Calcite	0.00	0.01	0.00	0.00	0	3	0	1	0	3	0	1
Chamosite	0.11	0.12	0.07	0.21	12	37	26	45	15	52	34	55
Muscovite	0.01	0.62	0.34	0.01	2	132	71	2	2	184	111	3
Amphibole	0.01	0.01	0.00	0.02	2	4	0	8	2	4	0	8
Yoderite	0.00	0.00	0.00	0.00	0	1	0	0	0	1	0	0
Tourmaline	0.01	0.01	0.04	0.00	2	6	9	0	2	6	10	0
Almandine-Mn	0.00	0.02	0.01	0.01	1	8	5	3	1	8	5	3
Almandine-Ca1	0.32	0.73	0.82	0.28	40	67	72	57	61	87	85	79
Almandine-Ca4	0.03	0.02	0.01	0.09	10	6	3	27	10	6	4	29
Almandine-Ca5	0.17	0.39	0.34	0.18	33	68	50	50	43	79	64	61
Almandine-Ca9	0.05	0.19	0.15	0.04	13	43	29	16	14	50	33	18
Grossular-Fe	0.00	0.01	0.02	0.00	0	3	5	0	0	4	6	0
Grossular	0.00	0.01	0.01	0.00	0	2	6	0	0	2	6	0
Spessartine-Ca	0.00	0.00	0.01	0.00	0	0	1	1	0	0	1	1
Spessartine	0.00	0.00	0.00	0.00	1	0	0	0	2	0	0	0
Spessartine-Fe	0.00	0.00	0.00	0.00	0	0	0	1	0	0	0	1
Magnetite	0.00	0.02	0.01	0.01	0	3	4	3	0	3	5	4
Magnetite-Ti	0.00	0.01	0.03	0.01	1	5	2	4	1	6	5	4
Ilmenite	0.00	0.01	0.00	0.01	1	2	2	2	1	2	2	2
Rutile	18.72	9.02	9.77	24.20	93	98	45	168	229	173	105	372
Chromite	0.00	0.00	0.00	0.00	0	0	0	0	0	0	0	0
Chromite-Mn	0.00	0.00	0.00	0.00	0	0	0	0	0	0	0	0
Titanite	24.71	63.53	73.27	46.23	143	564	250	350	400	740	363	761
Titanite-Fe	0.10	0.18	0.16	0.20	24	51	38	52	38	56	46	91
Zircon	55.09	19.10	10.03	26.83	165	169	45	123	166	178	46	124
Apatite	0.22	4.29	3.45	0.59	18	47	29	30	22	54	34	38
Barite	0.00	0.00	0.00	0.02	0	0	0	2	0	0	0	2
Monazite-Ce	0.00	0.00	0.00	0.00	0	0	0	1	0	0	0	1
NdLaCaThSmSiFeO	0.00	0.00	0.00	0.00	0	0	0	0	0	0	0	0
SiC	0.00	0.00	0.00	0.00	2	4	0	3	2	4	0	3
Unknown	0.00	0.00	0.00	0.00	2	4	0	1	2	6	0	1
Low_Counts	0.00	0.00	0.00	0.00	0	0	0	0	0	0	0	0
No_XRay	0.00	0.00	0.00	0.00	0	0	0	0	0	0	0	0
Total	100.00	100.00	100.00	100.00	289	777	304	474	1052	1878	1138	1744

Appendix D – XRD analysis

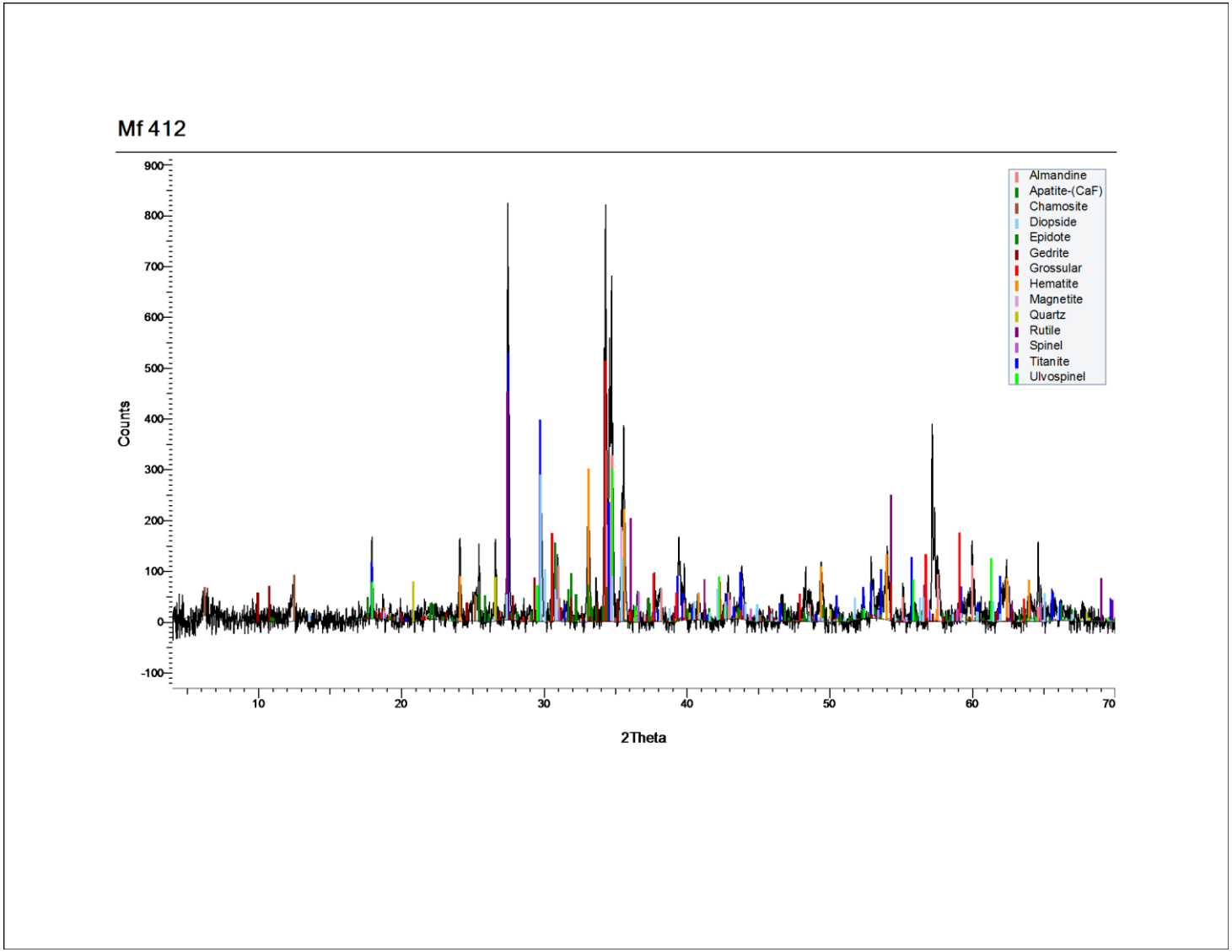

Mf 409

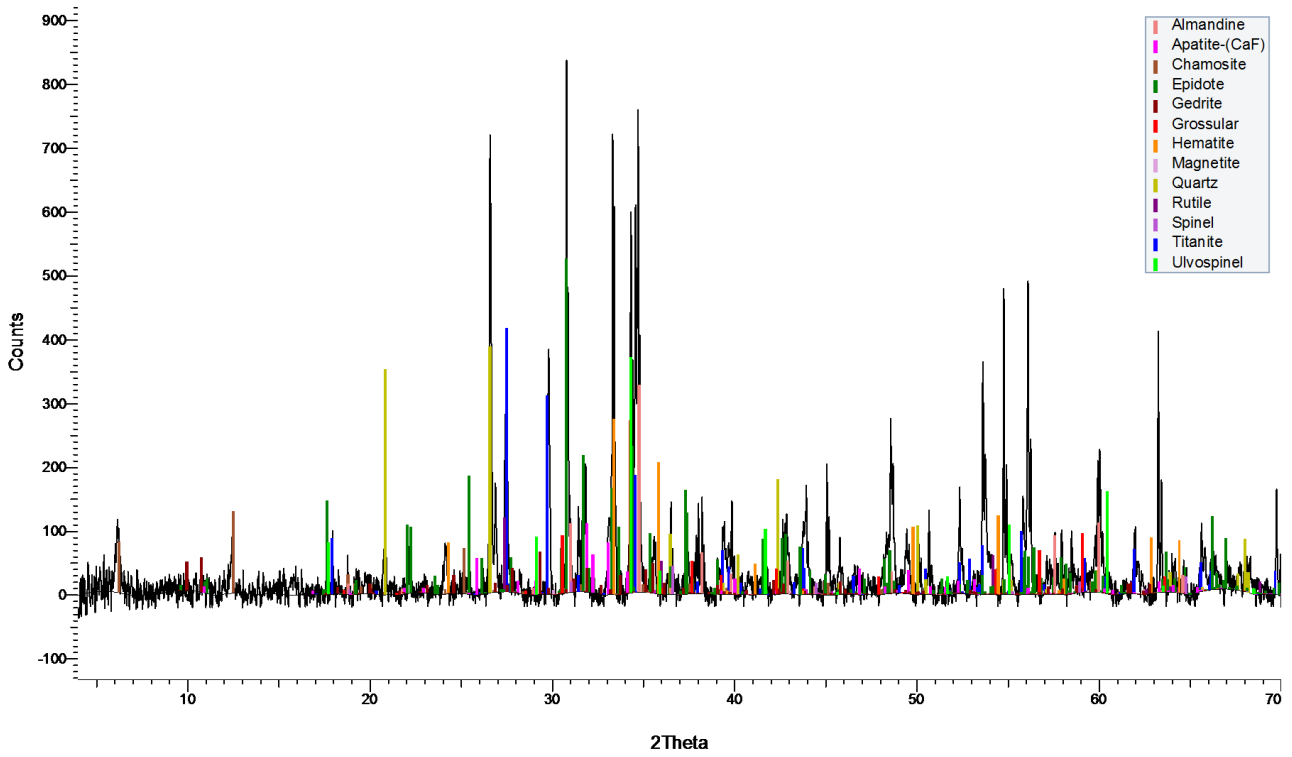
Almandine
Apatite-(CaF)
Chamosite
Epidote
Gedrite
Grossular
Hematite
Magnetite
Quartz
Rutile
Spinel
Titanite
Ulvospinel
Counts
900
800
700
600
500
400
300
200
100
0
-100
10
20
30
40
50
60
70
2Theta

Mf 408

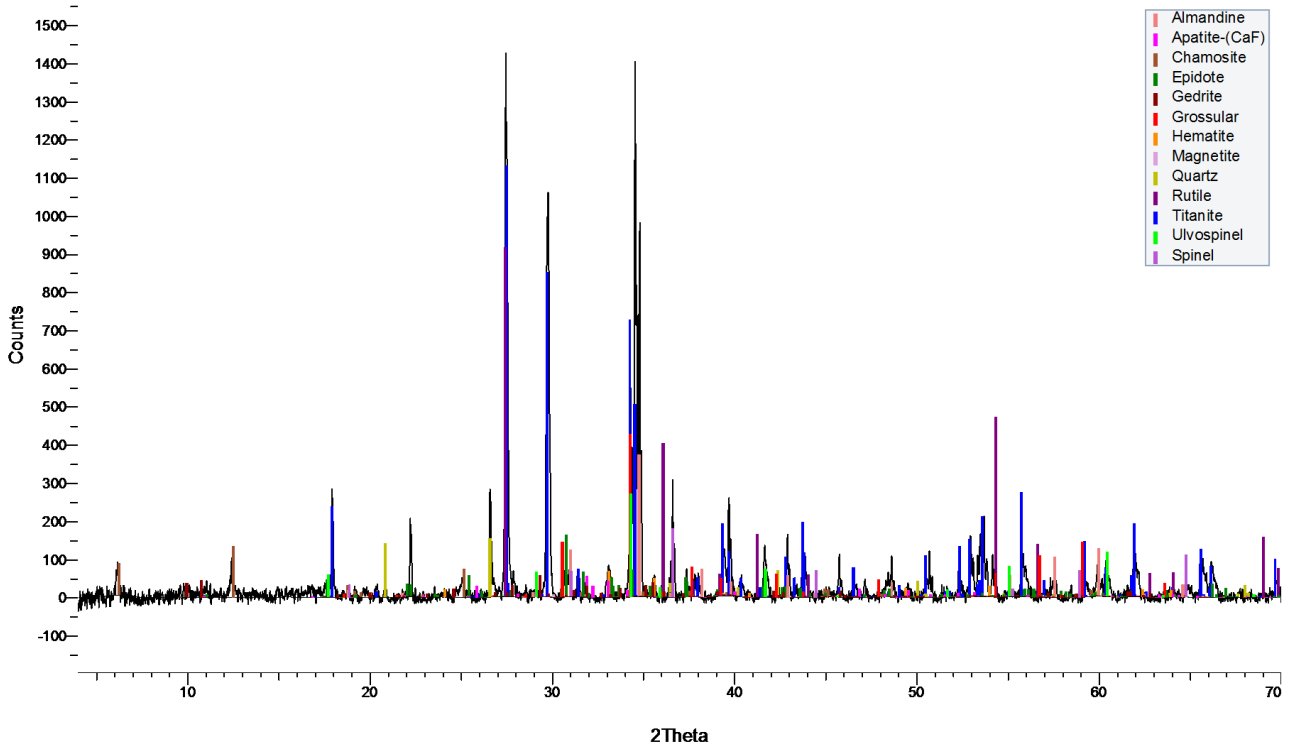
Almandine
Apatite-(CaF)
Chamosite
Epidote
Gedrite
Grossular
Hematite
Magnetite
Quartz
Rutile
Titanite
Ulvospinel
Spinel
Counts
1500
1400
1300
1200
1100
1000
900
800
700
600
500
400
300
200
100
0
-100
10
20
30
40
50
60
70
2Theta

Mf 405

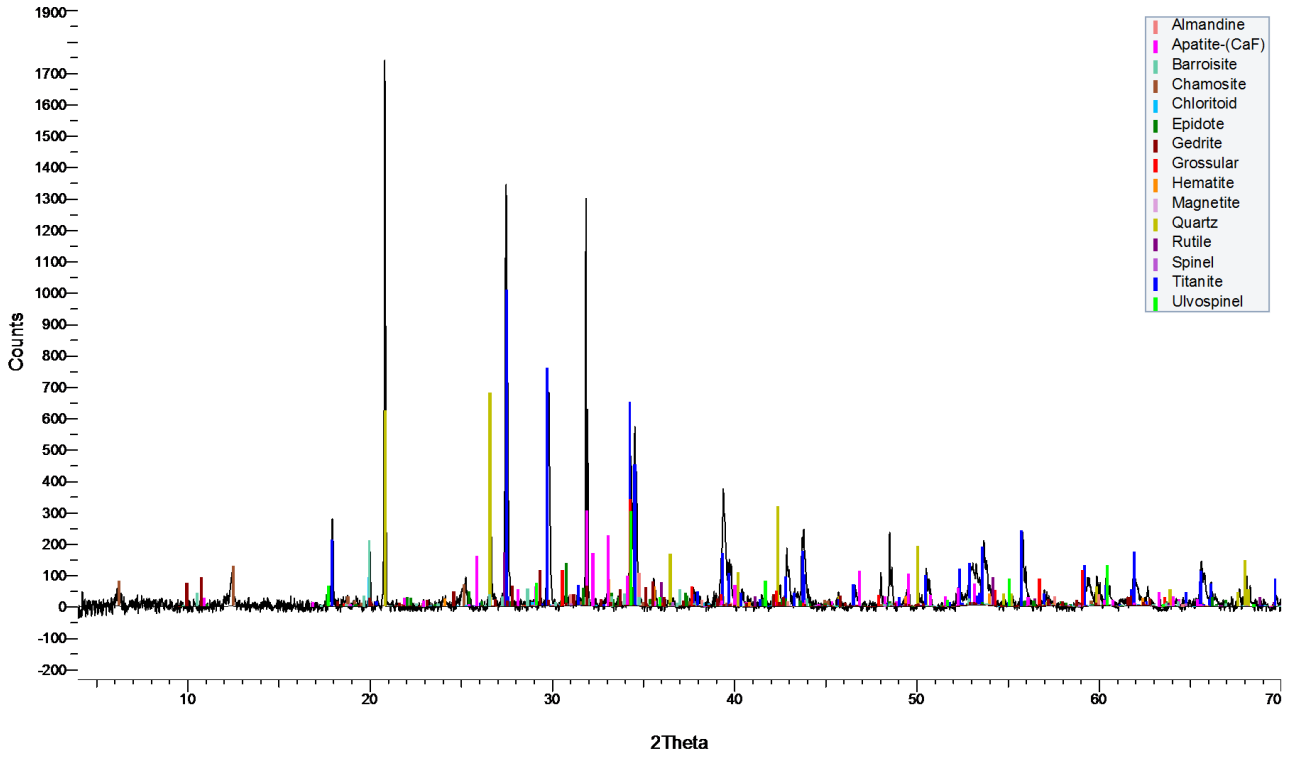
Almandine
Apatite-(CaF)
Barroisite
Chamosite
Chloritoid
Epidote
Gedrite
Grossular
Hematite
Magnetite
Quartz
Rutile
Spinel
Titanite
Ulvospinel
Counts
1900
1700
1600
1500
1400
1300
1200
1100
1000
900
800
700
600
500
400
300
200
100
0
-100
-200
10
20
30
40
50
60
70
2Theta

Ap 412

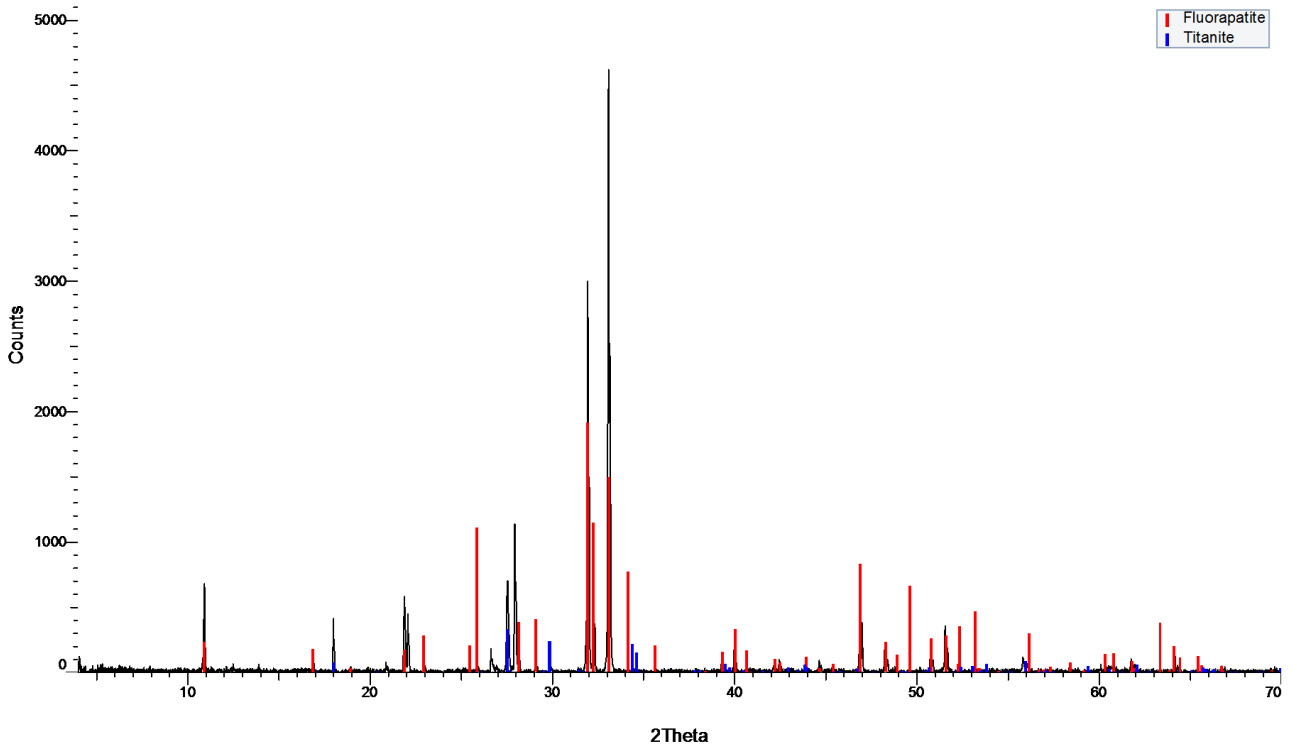
Fluorapatite
Titanite
Counts
5000
4000
3000
2000
1000
0
10
20
30
40
50
60
70
2Theta

Ap 409

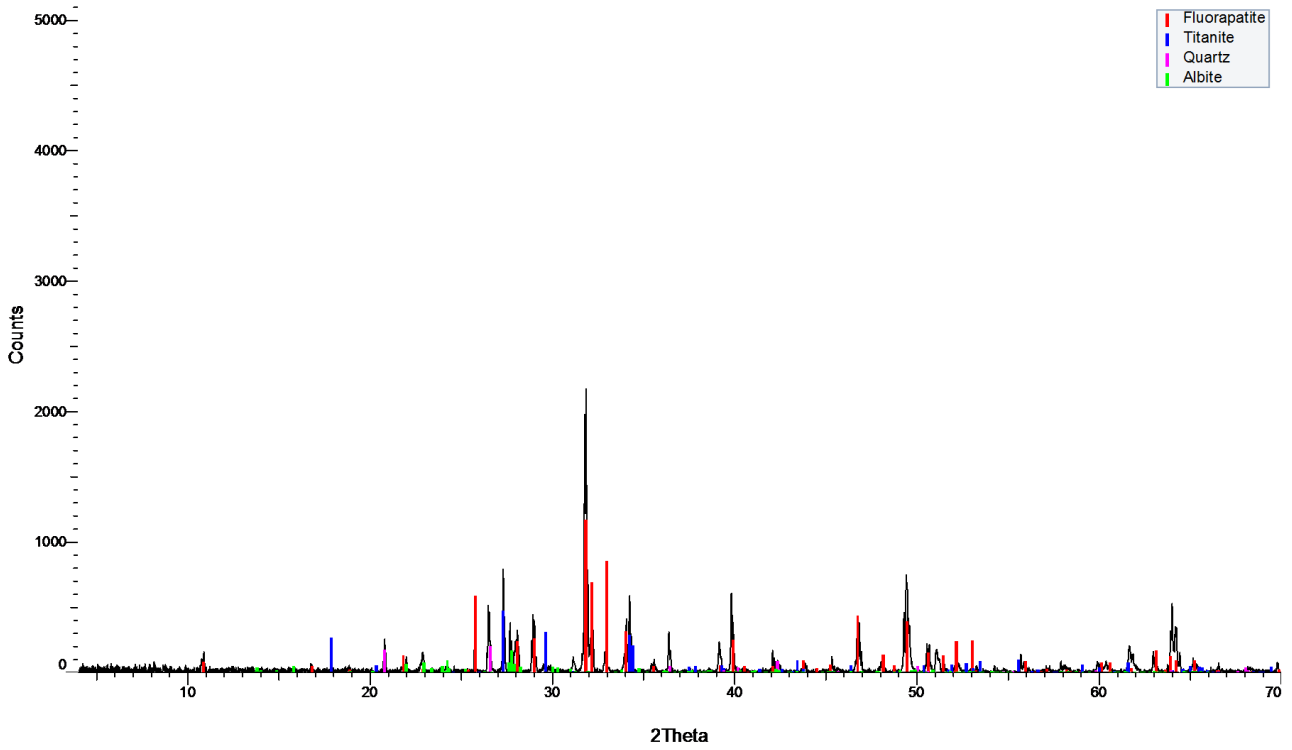
Fluorapatite
Titanite
Quartz
Albite
Counts
5000
4000
3000
2000
1000
0
10
20
30
40
50
60
70
2Theta

Ap 408

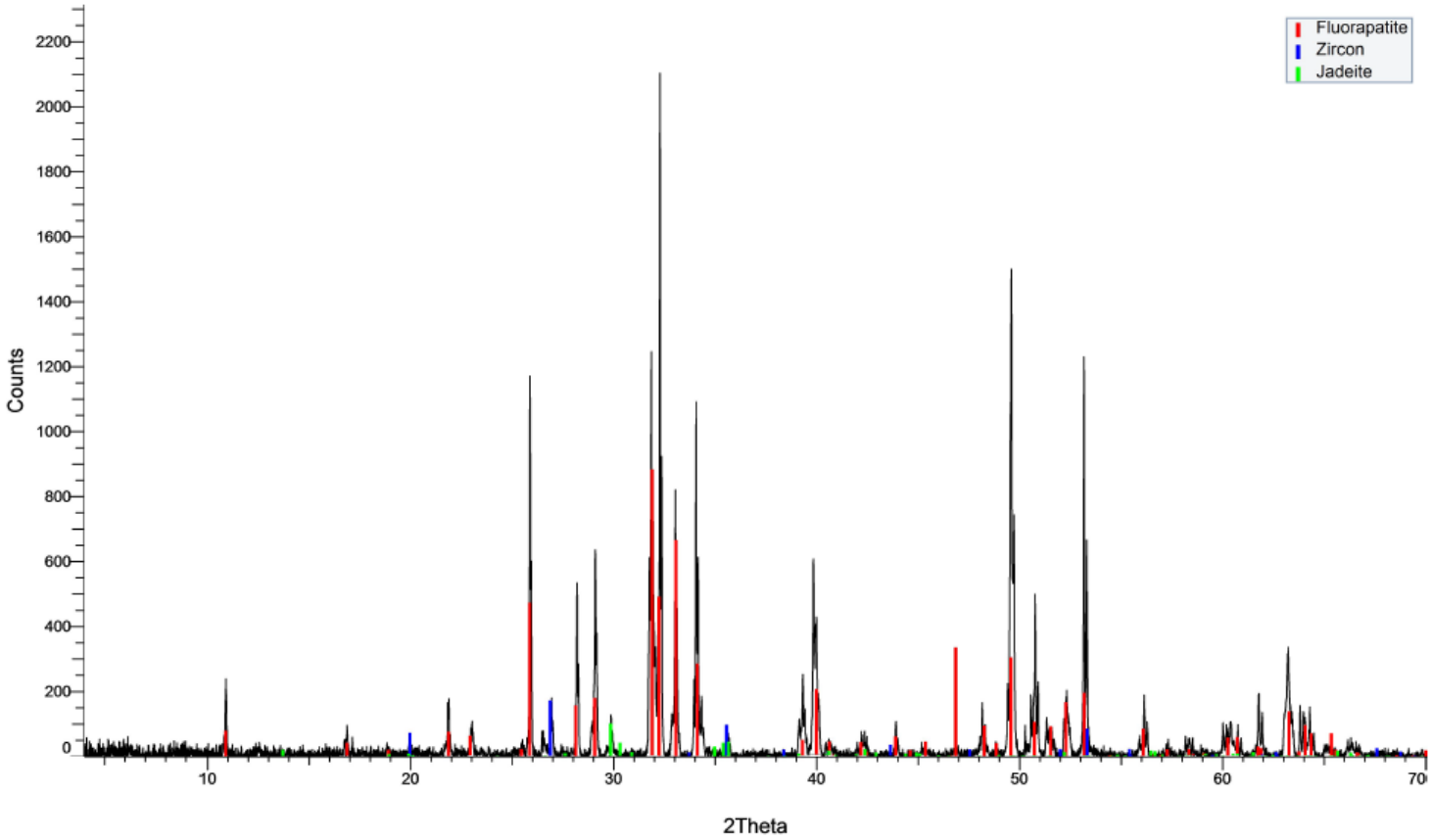
Fluorapatite
Zircon
Jadeite
Counts
2200
2000
1800
1600
1400
1200
1000
800
600
400
200
0
10
20
30
40
50
60
70
2Theta

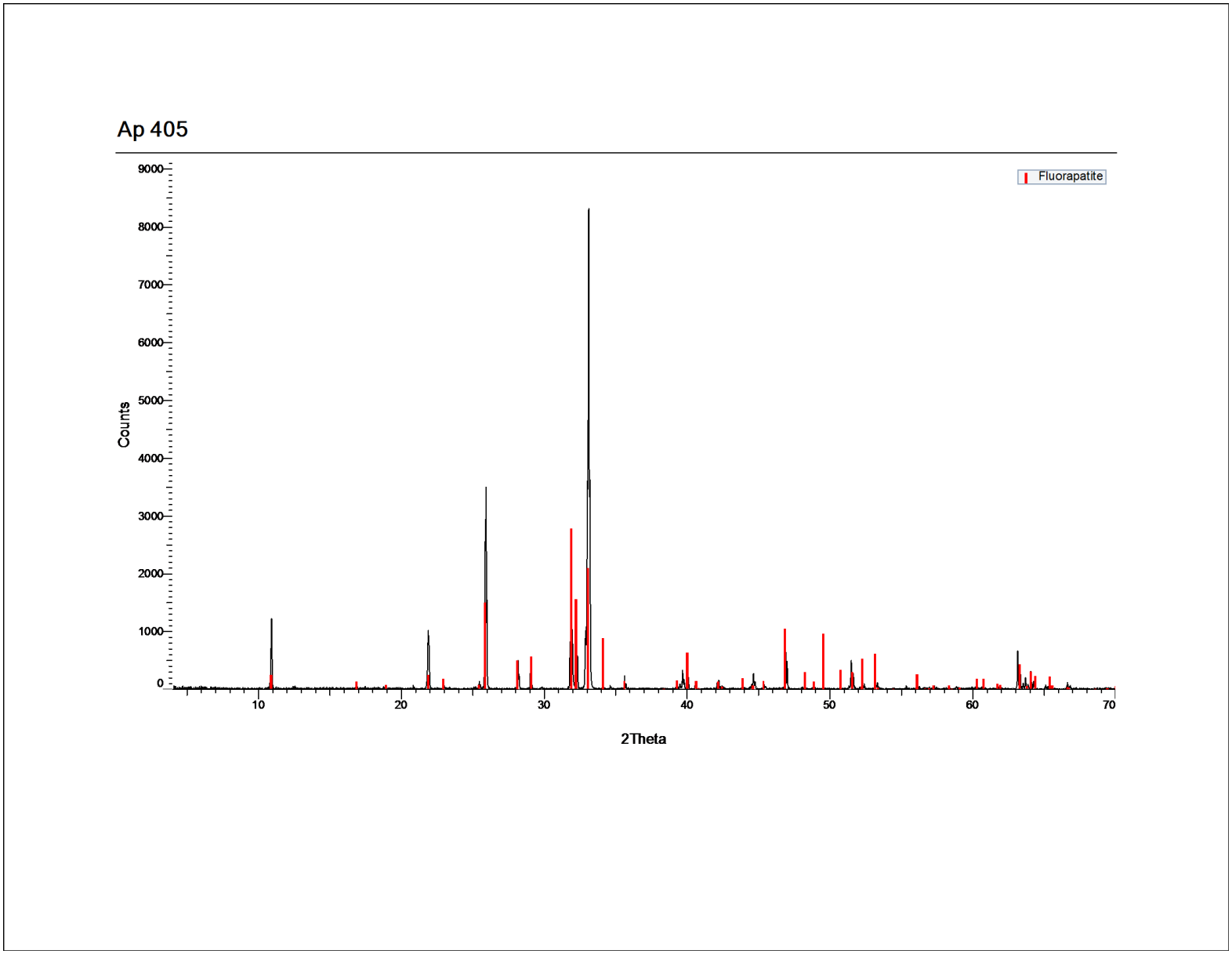
Ap 405
Fluorapatite
Counts
9000
8000
7000
6000
5000
4000
3000
2000
1000
0
10
20
30
40
50
60
70
2Theta

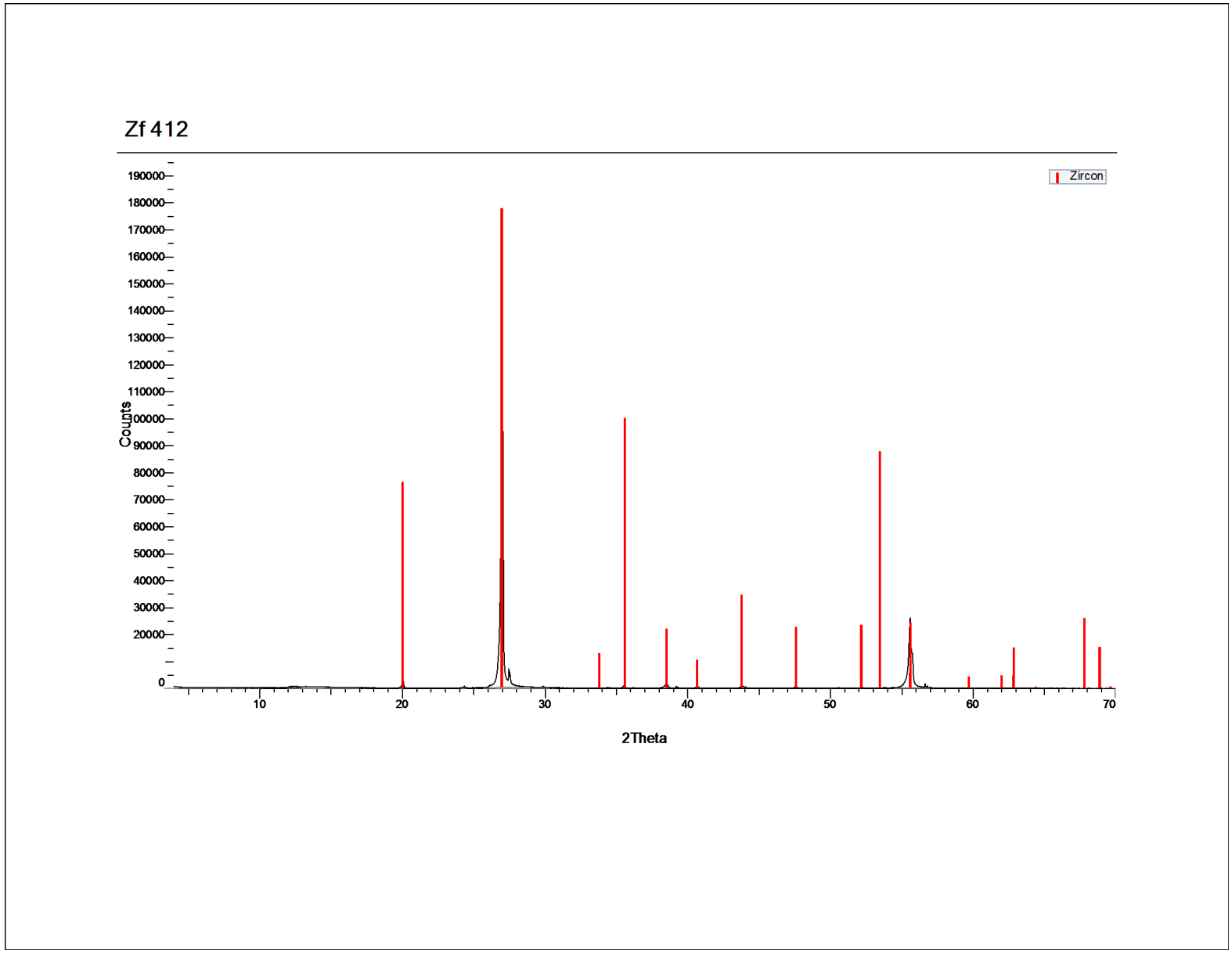
Zf 412
Zircon
Counts
2Theta
0
20000
30000
40000
50000
60000
70000
80000
90000
100000
110000
120000
130000
140000
150000
160000
170000
180000
190000
10
20
30
40
50
60
70

Zf 409

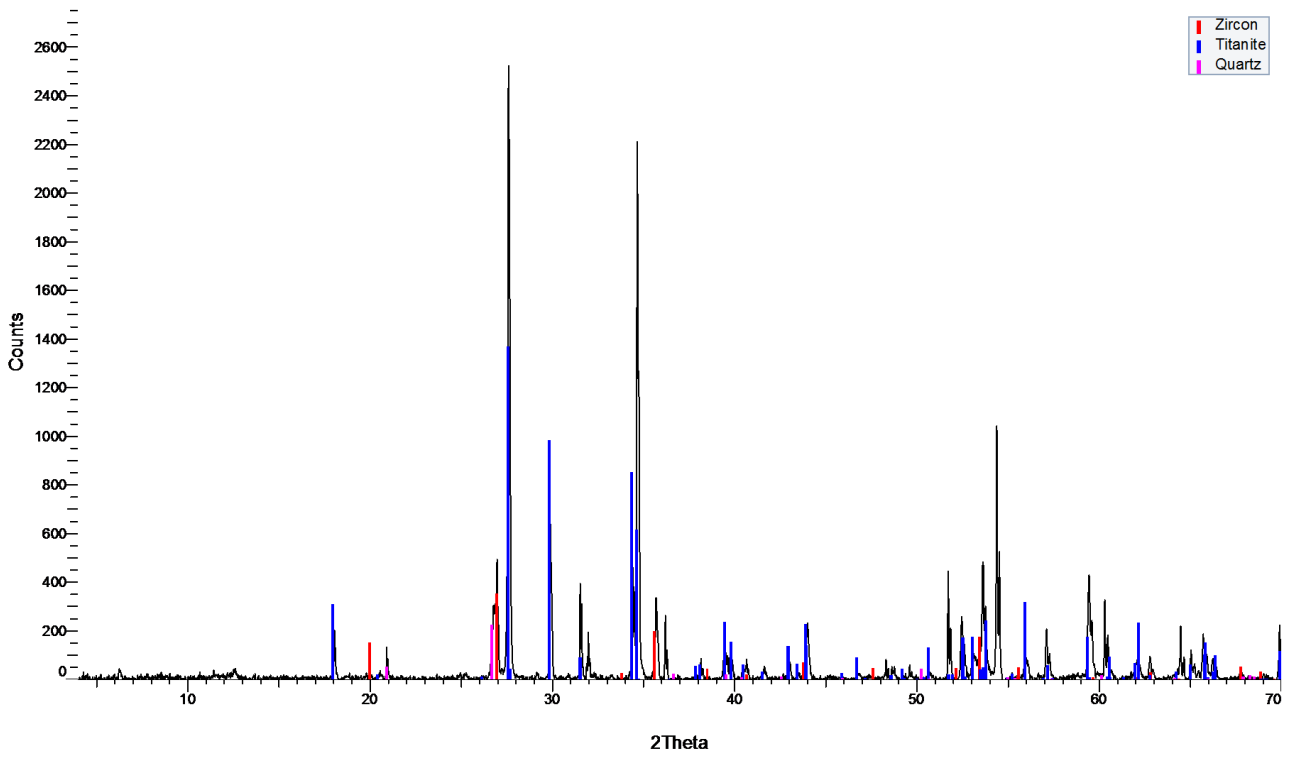
Zircon
Titanite
Quartz
Counts
2Theta
0
200
400
600
800
1000
1200
1400
1600
1800
2000
2200
2400
2600
10
20
30
40
50
60
70

Zf 408

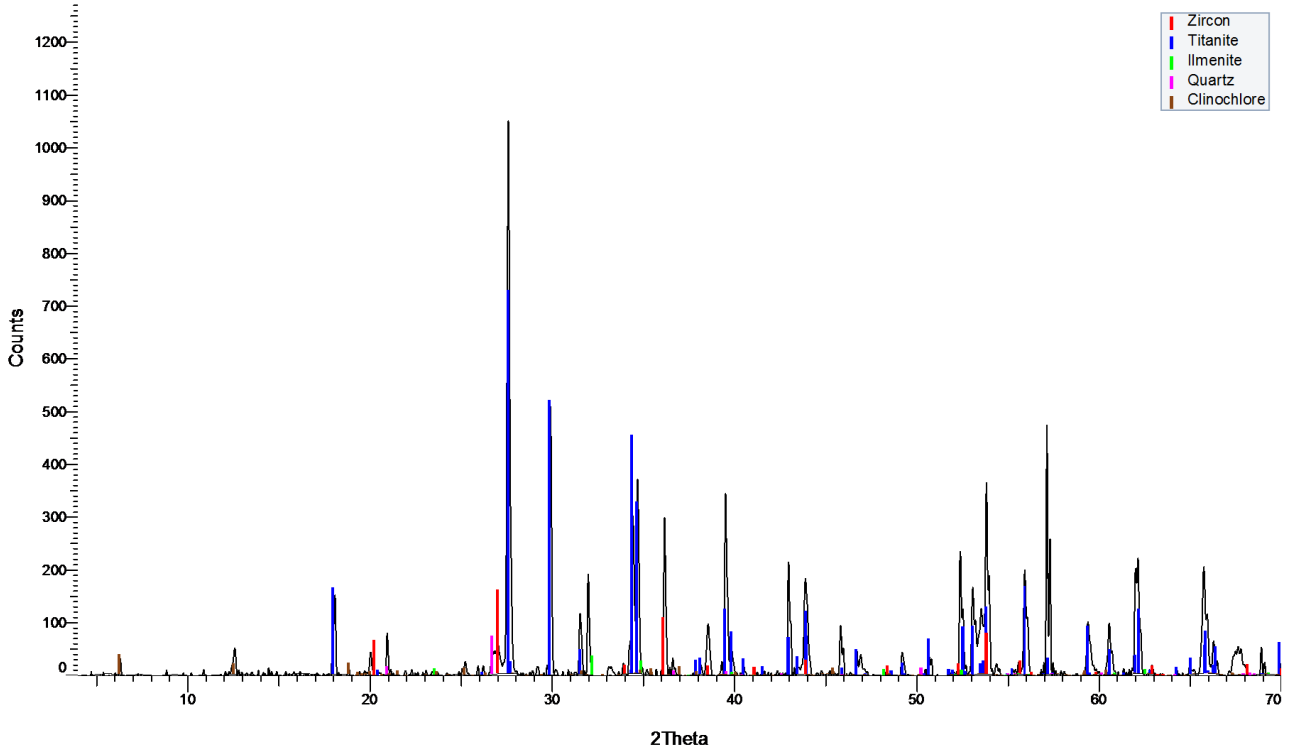
Zircon
Titanite
Ilmenite
Quartz
Clinochlore
Counts
2Theta
0
100
200
300
400
500
600
700
800
900
1000
1100
1200
10
20
30
40
50
60
70

Zf 405

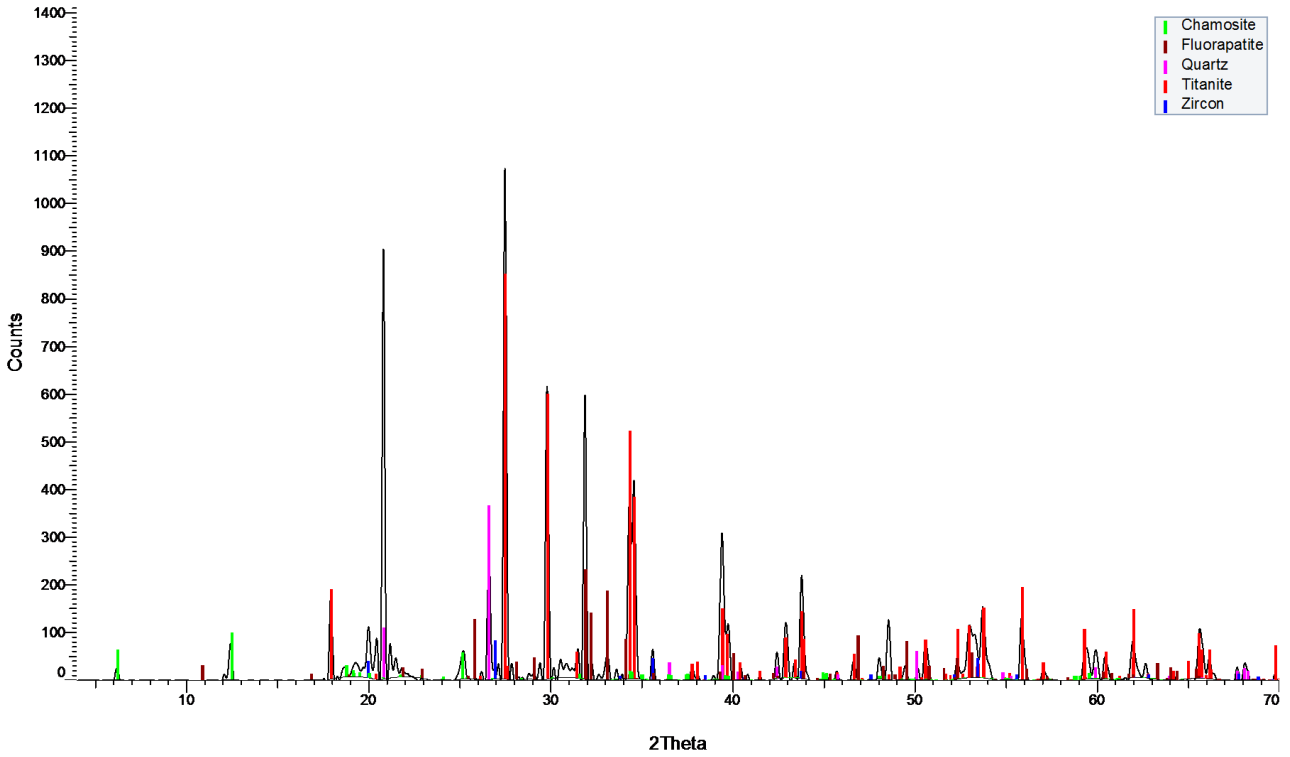
Chamosite
Fluorapatite
Quartz
Titanite
Zircon
Counts
2Theta
0
100
200
300
400
500
600
700
800
900
1000
1100
1200
1300
1400
10
20
30
40
50
60
70